LLNL-JRNL-2000221

Glacial to periglacial transition at the end of the last ice age in the subtropical semiarid Andes

A. Hidy, J. Garcia, J. Carraha, H. Fernandez-Navarro, F. Perez, S. Nussbaumer, I. Gartner-Roer, W. Haeberli

November 2024

This work performed under the auspices of the U.S. Department of Energy by Lawrence Livermore National Laboratory under Contract DE-AC52-07NA27344.

LLNL-JRNL-2000221

Lawrence Livermore National Laboratory

Glacial to periglacial transition at the end of the last ice age in the subtropical semiarid Andes

Unclassified (unlimited audience)

September 13, 2024

Disclaimer

Lawrence Livermore National Laboratory is operated by Lawrence Livermore National Security, LLC, for the U.S. Department of Energy, National Nuclear Security Administration under Contract DE-AC52-07NA27344.

Glacial to periglacial transition at the end of the last ice age in the subtropical semiarid Andes

Juan-Luis García [a,b,*], Javiera Carraha [a,b], Hans Fernández-Navarro [c], Samuel U. Nussbaumer [d], Francia Pérez [a], Alan J. Hidy [e], Isabelle Gärtner-Roer [d], Wilfried Haeberli [d]

[a] Instituto de Geografía, Facultad de Historia, Geografía y Ciencia Política, Pontificia Universidad Católica de Chile, Av. Vicuña Mackenna 4860, Macul, Santiago, Chile
[b] Centro UC Desierto de Atacama, Pontificia Universidad Católica de Chile, Santiago, Chile
[c] Instituto de Ciencias Agroalimentarias, Animales y Ambientales (ICA3), Universidad de O'Higgins, San Fernando, Chile
[d] Department of Geography, University of Zurich, Zurich, Switzerland
[e] Center for Accelerator Mass Spectrometry, Lawrence Livermore National Laboratory, Livermore, CA 94550, USA

A B S T R A C T

Atmospheric warming and circulation reorganization at the end of the last ice age represent the most important climate change of the last 100,000 years and provide an opportunity to uncover how the southern subtropics cryosphere responded to strong changes in the global climate system. Extensive mapping and chronologic records on cryogenic landforms to better understand the association and interactions between glaciers and viscous creep of ice-rich permafrost landforms (rock glaciers) are widely missing in the region. In this paper, we reconstruct the geomorphic imprint of the Last Glacial Maximum (LGM) and the Termination I in the high Andes of the Río Limarí Basin (30–31°S) in the subtropical semiarid Andes of Chile. 74 new ^{10}Be surface exposure dating ages constrain the timing of glaciation, deglaciation, and glacial to periglacial transition. Glacial advances occurred first by 41.2 ± 0.6 – 35.0 ± 0.5 ka during Marine Isotope Stage 3, but probably earlier also; then, a second advance occurred during the global LGM between 24.2 ± 0.4 and 18.6 ± 0.2 ka. Deglaciation by 17.6 ± 0.2 ka left extensive hummocky moraines on the main valleys. Characteristic patterns of furrows and ridges typical of rock glaciers and solifluction superimposed on the LGM hummocky moraine indicate ice-rich permafrost in glacial deposits likely between 15.5 ± 0.3 and 13.6 ± 0.3 ka. We propose that moraines deposited by LGM debris-covered glaciers served as a niche for strong seasonal frost and permafrost creep, which substantially modified the original landforms. Our results contribute to a better understanding of major transformations in an ice-rich high mountain area of the southern hemisphere where the interplay of temperature and precipitation changes drove glacial to periglacial transitions.

1. Introduction

The glacial and periglacial geomorphic record of high mountains, such as in the subtropical Andes (Zech et al., 2006, 2007; García et al., 2017; Carraha et al., 2024) and elsewhere, provides a unique opportunity to assess the cryosphere response to climate change (Clark et al., 1996; Shroder et al., 2000; Frauenfelder and Kääb, 2000; Ballantyne, 2002; Matthews et al., 2017; Amschwand et al., 2021; Palacios et al., 2021). The Termination I (c. 18–11.5 ka) embraced an abrupt global reorganization of the ocean and atmosphere circulation patterns (Denton et al., 2010; Palacios et al., 2022) but there is limited knowledge on how ice-rich high mountains and associated cryo-geomorphic processes evolved from the Late-Pleistocene to the Holocene (Oliva et al., 2021). Reconstructing the mountain cryo-geomorphic processes during the Termination I can add valuable understanding of the future of ice-rich high mountains with global warming (Hock et al., 2022). In this paper, we aim to reconstruct the glacial and periglacial geomorphic processes that resulted from global climate change at the end of the last glaciation in the Río Limarí Basin (30–31° S) in the subtropical semiarid Andes of Chile (Figs. 1 and 2). Here, Late Pleistocene glacier downwasting and retreat and the evolution of ice-rich permafrost have left a distinct geomorphic imprint that we have

* Corresponding author at: Instituto de Geografía, Facultad de Historia, Geografía y Ciencia Política, Pontificia Universidad Católica de Chile, Av. Vicuña Mackenna 4860, Macul, Santiago, Chile.

E-mail address: jgarciab@uc.cl (J.-L. García).

mapped in detail (Carraha et al., 2024). We support our analysis with 74 new ^{10}Be surface exposure dates of cryogenic landforms (e.g., moraines).

Glaciers and permafrost are primary components of the high-mountain cryosphere (Haeberli and Burn, 2002). Where the glacier equilibrium-line altitude (ELA) intersects the relief, glaciers form and where the ELA is above the relief, ice-rich permafrost-related phenomena such as rock glaciers can develop and predominate if certain environmental conditions are met (Haeberli and Beniston, 1998). Whereas glaciers depend on positive snow/ice mass balance to form and expand, rock glaciers depend on the growth and long-term preservation of subsurface ice (interstitial, segregation or massive ice) inside rock debris, forming a cohesive ice-rock mixture with reduced internal friction that deforms by steady-state creep in response to gravity in a permafrost environment with negative – sometimes near 0 °C - mean air annual temperature (MAAT) (Haeberli and Vonder Mühll, 1996; Trombotto et al., 1997; Etzelmüller and Frauenfelder, 2009; Matthews et al., 2017). The distribution of permafrost occurs at lower elevations under maritime climates where summer temperatures are moderate and favor ground ice preservation, in places even with slightly positive MAATs (Brenning, 2005; Sattler et al., 2016). The climatically sensitive elevation of the ELA and MAAT determines the development of glacial and periglacial landforms that represent former climate fluctuations through time within the high-mountain realm (Brenning, 2005; Hendrickx et al., 2015). Glacial to periglacial transitions embrace important cryogenic changes in the mountain environment in response to warming and/or decreasing precipitation driving a higher ELA and MAAT (Haeberli and Burn, 2002). For instance, valleys formerly occupied by glaciers in the Late Pleistocene may have become occupied by ice-rich permafrost-related viscous creep features (rock glaciers) in the Holocene (Lehmann et al., 2022). Similarly, present-day degradation of glaciers after the last maximum of the Little Ice Age (LIA), the period of a few centuries between the Middle Ages and the warming of the first half of the 20th century, as recorded in the northern hemisphere, can be accompanied by the development of periglacial landforms under permafrost conditions (Seppi et al., 2014; Colombo et al., 2016). Thereby, ice-rich permafrost undergoing viscous creep in cases and over extended time scales of millennia can lead to the formation of often spectacular rock glaciers, which can sometimes appear spatially associated with glacial deposits and remains of glaciers, thus forming complex composite features (Monnier et al., 2014; Vivero et al., 2021; Gärtner-Roer et al., 2022; Haeberli et al., 2024). Through slow/deep freezing and subsurface ice formation, unconsolidated sediments (talus, debris) with essentially zero cohesion and high internal friction can transform into coherent viscous creep features and periglacial rock glaciers (Matthews et al., 2017). The process of covering ice with debris alone cannot produce characteristic "rock-glacierized" viscous flow structures with talus-type oversteepened fronts (cf. the detailed discussion about material properties and related processes in Haeberli et al. (2024): Glaciers may contribute with rock material and sometimes remains of dead ice to creeping frozen bodies (Barsch (1996) but cannot themselves "become" rock glaciers)).

The subtropical Andes are situated at the present-day northern boundary of the Southern Westerly Wind belt (SWW), which exerts direct control on regional precipitation and glacier fluctuations (Garreaud, 2009; Fernández-Navarro et al., 2023). Thus, the study area is climatically sensitive to the latitudinal migration of these winds in link to the Southern Ocean circulation and sea-ice extent (Lamy et al., 2015). Main climate shifts and glacier fluctuations throughout the last glacial period have been associated with the SWW latitudinal position and strength, although limited paleoglaciological knowledge exists for the Andean subtropics (Fig. 1) (Stuut and Lamy, 2004; Veit et al., 2015;

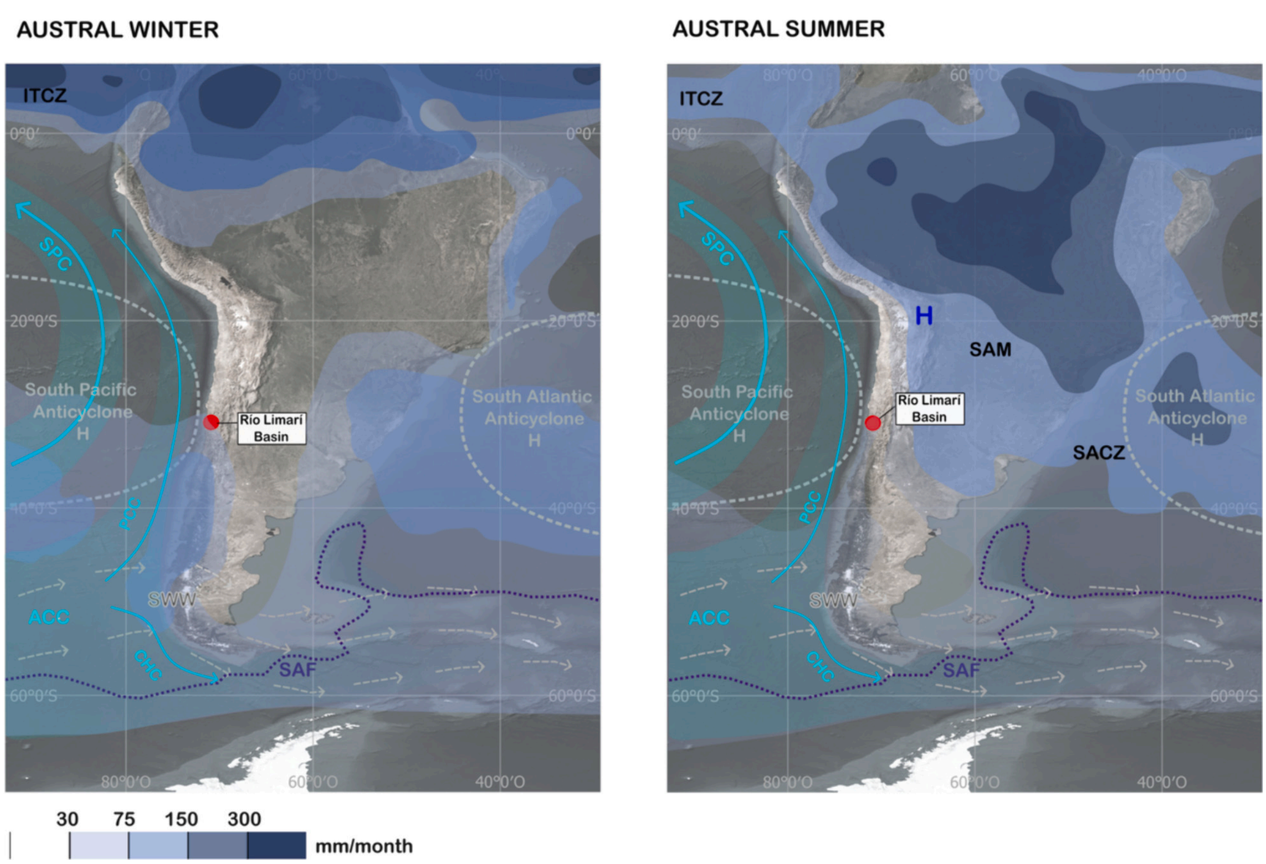

Fig. 1. Regional scale present-day mean surface precipitation. Ocean and atmospheric circulation patterns for the study area after Garreaud (2009); Lamy et al. (2015); Veit et al. (2015). SWW: Southern Westerly Wind; SPC: South Pacific Current; PCC: Perú-Chile Current; ACC: Antarctic Circumpolar Current; CHC: Cape Horn Current; SAF: Sub-Antarctic Front.

García et al., 2018, 2019; Gómez et al., 2022; Lira et al., 2022). For instance, Zech et al. (2006, 2007, 2017) dated moraines using ^{10}Be surface exposure technique in the Río Limarí (31° S) and Río Huasco (29° S) Andean Basins. In Limarí (Cordón Doña Rosa site) several moraine ridges were mapped and dated with ^{10}Be ages ranging c. 50–40 ka in the outer moraines and c. 26–18 ka in the inner moraines (Zech et al., 2017). In Huasco, several moraine ridges were deposited in the El Encierro Valley between 26 and 18 ka, although previous advances cannot be ruled out (Zech et al., 2017; Aguilar et al., 2022). In a recent study, Charrier et al. (2019) obtained two ^{10}Be exposure ages between c. 20–22 ka for the Cerrillos moraine in the Río Rapel Basin, 34° S (Santana, 1967). Glaciers in Huasco retreated by 18 ka, but in Rapel and Maipo they readvanced during the Late-glacial period (c. 14–10 ka) (Fernández et al., 2021; Herrera-Ossandón et al., 2023). In our study, we discuss the new geomorphic and ^{10}Be surface exposure dating geochronologic reconstruction in link to past SWW latitudinal migration during the Last Glacial Maximum (LGM) and Termination I. Particular emphasis is given on the timing of glaciation, deglaciation, and glacial to periglacial transition denoted by the geomorphic imprint of the Limarí Andes, which was mapped and described in detail by Carraha et al. (2024).

2. Study area

The subtropical Andes are a rugged terrain dominated by towering mountains with elevations exceeding 6000 m a.s.l., although in the Limarí Basin, our study area, summits reach about 4000 m a.s.l. (Co. Cenicero, 4114 m a.s.l.) in the south and above 5000 m a.s.l. in the north. The Andean landscape is distinguished by widespread valleys sculpted by ancient glaciers, showcasing remarkably well-preserved glacial and periglacial features (Caviedes and Paskoff, 1975; Paskoff, 1977; Espizua, 1993; García et al., 2014; Zech et al., 2017; Charrier et al., 2019). Similarly, the U-shaped valleys and moraines in the Andes of Limarí denote the imprint of Quaternary glaciations (Zech et al., 2007, 2017; Carraha et al., 2024). At present, only few and small glaciers remain in the Limarí Basin covering ~2.6 km^2 in extent, much less than intact rock glaciers covering an area of ~25.6 km^2 as inventoried by the Dirección General de Aguas (2022). To date, no inventories exist for the study area that differentiate between active (containing ice and moving) and inactive (containing ice and rather no movement) rock glaciers. Nonetheless, clear indications of active permafrost creep can be observed – where topographically not confined – on cold south-exposed slopes down to about 3600 m a.s.l. The ELA for glaciers in Limarí is at 5100–5300 m a.s.l., i.e., far above the 0 °C MAAT at about 3800 m a.s.l. and the associated lower discontinuous permafrost limit, denoting the effect of limited precipitation in the area (Azócar and Brenning, 2010; Haeberli and Burn, 2002). The remaining glacierets and perennial ice patches are therefore likely to be surrounded by permafrost and be cold, frozen to their beds.

A significant precipitation latitudinal gradient exists in this part of the Andes controlled by the SWW with annual totals of ~300 mm in the north by 31° S (the Limarí Basin) and ~1000 mm in the south by 34° S (Masiokas et al., 2020). Precipitation falls mainly during the southern winter between May and August (80 % of the annual total), coincident with a reduced South Pacific Anticyclone blocking effect that allows storm tracks to reach the area (Vicuña et al., 2011; Quintana and Aceituno, 2012; Sagredo and Lowell, 2012). The semiarid conditions plus the intense insolation determine that glaciers are rather sensitive to the limited precipitation they receive (Zech et al., 2008; Sagredo and Lowell, 2012). At interannual time scales, precipitation and glacier mass balance follow the El Niño-Southern Oscillation (ENSO) (Vicuña et al., 2011; Quintana and Aceituno, 2012; Masiokas et al., 2020), although long-term positive mass balance and glacier advances have been associated with the Southern Annular Mode (SAM), suggesting its control over the position of the SWW and precipitation rates (Fernández-Navarro et al., 2023).

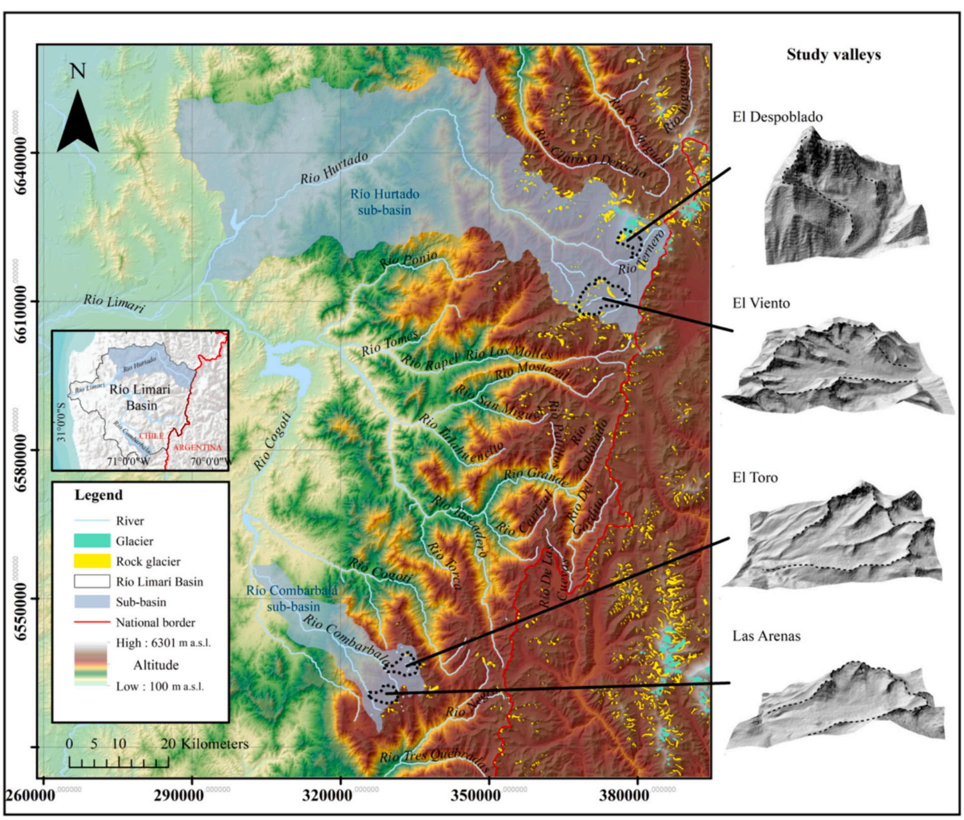

Fig. 2. The Limarí River Basin depicting the topographic detail of each of the studied valleys. Rock glacier and glacier information based on Dirección General de Aguas (2022) in Chile and Instituto Argentino de Nivología (2018) in Argentina.

3. Materials and methods

Our investigation is based on the detailed geomorphological mapping as presented in Carraha et al. (2024). We selected two sub-basins at the northern and southern limits of the Limarí catchment, in which glacial and periglacial processes were studied: The Río Hurtado and Río Combarbalá sub-basins, respectively. Two valleys were selected in each of the sub-basins: El Viento (EV, 30°38′ S; ~3300–4400 m a.s.l.) and El Despoblado (ED, 30°31′ S; ~3600–5300 m a.s.l.) from Río Hurtado, and El Toro (TOR, 31°17′ S; ~2700–4000 m a.s.l.) and Las Arenas (LAR, 31°20′ S; ~2900–3800 m a.s.l.) from Río Combarbalá (Fig. 2). We selected these valleys because they contain a well-preserved glacial and periglacial geomorphic record with suitable quartz-rich granodioritic lithology (SERNAGEOMIN, 2006) to produce our ^{10}Be geochronology. In the following, we therefore provide a regional perspective of past cryospheric and climatic changes for the subtropical semiarid Andes.

Geomorphological analysis and sampling for ^{10}Be cosmogenic exposure dating was carried out during four field campaigns to the study area during January 2020, 2022, 2023, and November 2020. Landform identification was also achieved by extensive analysis of ESRI BaseMap and Google Earth satellite images, as well as of aerial photographs at the scale of 1:50000 obtained by the Servicio Aerofotogramétrico de Chile (SAF). All elevations and locations were measured with a hand-held GPS unit. As a result, we built four geomorphic maps integrating both the field and image-based data, which served as base for our geochronological interpretation (Figs. 3–7) (Carraha et al., 2024).

To constrain the age of glacial advances, the timing of glacier retreat and landscape transformation at the Pleistocene-Holocene transition we applied ^{10}Be surface exposure dating. We targeted 74 samples from the top of quartz-rich granodiorite boulders that were embedded or resting on top of moraines in all four of the studied valleys: El Toro, Las Arenas, El Viento, and El Despoblado valleys. We followed standard protocols for rocks sampling and processing (Fernández-Navarro et al., 2023). Boulders were either embedded or resting in apparent stable positions on the surface of moraines. Whenever possible we sampled well-preserved polished boulders generally >50 cm high, with limited signs of postglacial erosion. We preferred boulders preserving signs of subglacial abrasion with subrounded faceted shapes, in some cases preserving the original outer glacially polished surface so to minimize possible inheritance of ^{10}Be from previous surface-exposure histories.

Samples were collected from the main axis of the outer lateral moraine ridges, outer and inner ridges punctuating hummocky moraine surface, line of boulders marking the former margin of glaciers, and group of boulders and till mantling the top of distinct valley bottom

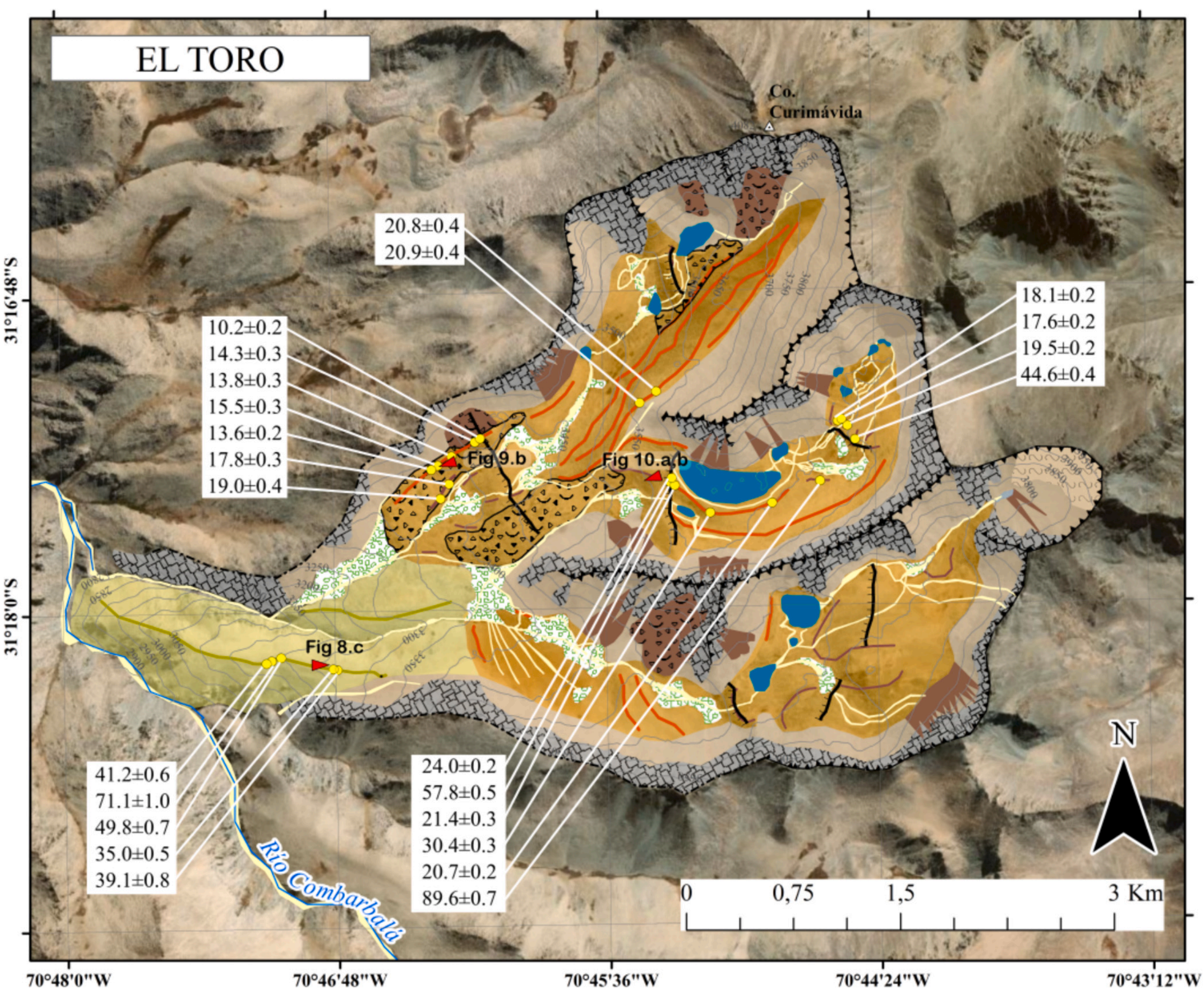

Fig. 3. ^{10}Be ages (in thousands of years ago; error 1 sigma) of rock samples from LIM I and LIM II moraines in the El Toro Valley, Andean highlands of the Río Limarí Basin. Base geomorphic map from Carraha et al. (2024). Red triangular arrows indicate the locations where photos were taken and the direction the camera was pointing.

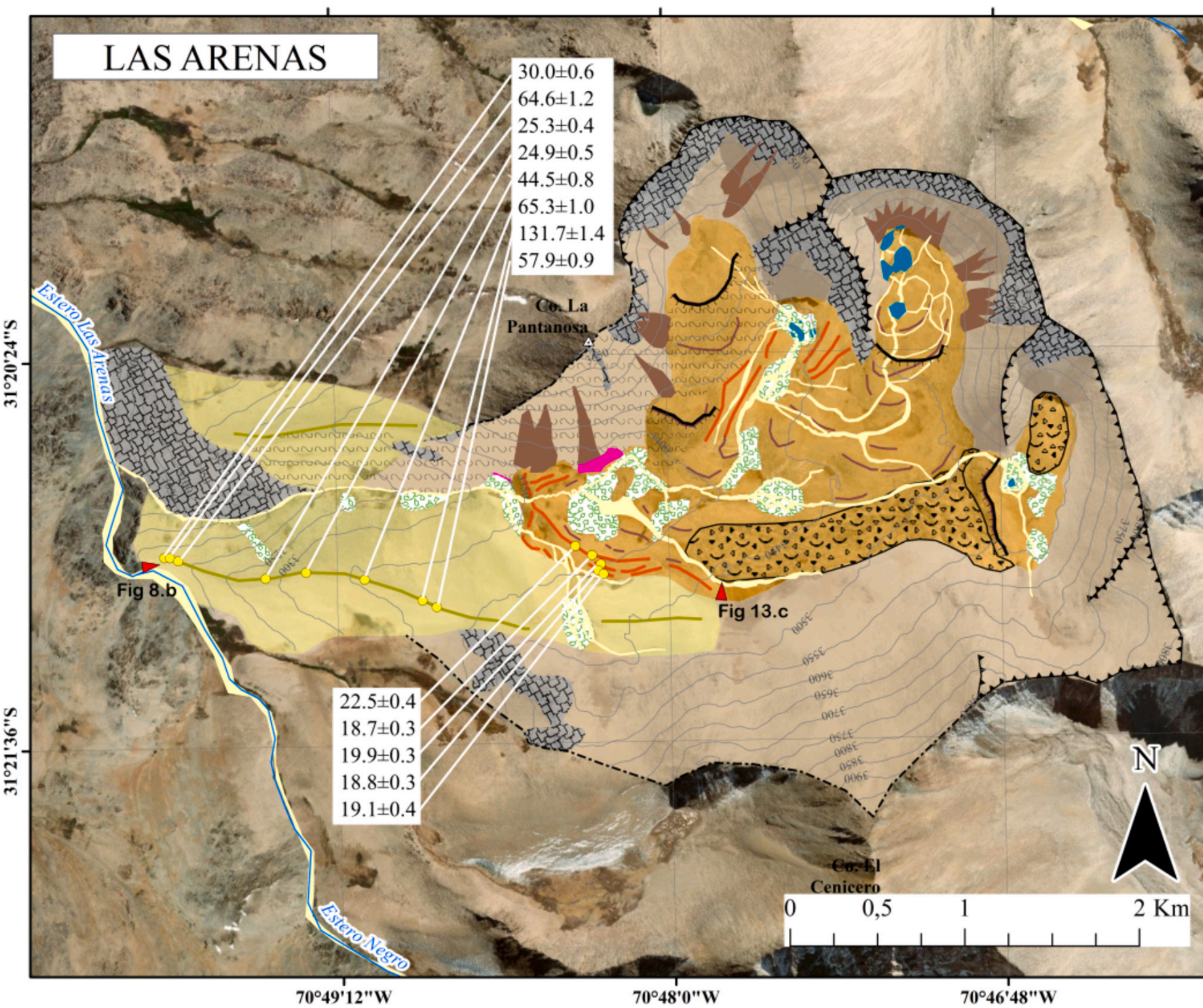

Fig. 4. ^{10}Be ages (in thousands of years ago; error 1 sigma) of rock samples from LIM I and LIM II moraines in the Las Arenas Valley, Andean highlands of the Río Limarí Basin. Base geomorphic map from Carraha et al. (2024). Red triangular arrows indicate the locations where photos were taken and the direction the camera was pointing.

topographic thresholds (i.e., rock steps). We sampled rock surfaces using hammer and chisel, blasts, and a handheld circular saw to collect the rock samples.

Rock samples were processed at the *Laboratorio de Isótopos Cosmogénicos y Paleoclima del Cuaternario at the Universidad Católica de Chile*, where clean quartz was extracted from the samples and ^{10}Be isolated following a procedure adapted from standard protocols (Kohl and Nishiizumi, 1992). Targets for ^{10}Be/^{9}Be ratios were measured at the Center for Accelerator Mass Spectrometry (CAMS) at Lawrence Livermore National Laboratory (LLNL). We used the southern Andes ^{10}Be production rate by Kaplan et al. (2011), and Version 3 of the online calculators (Balco et al., 2008) to compute exposure dates (Tables 1 and 2). We discussed our ages using the time-dependent Lm scaling scheme (Lal, 1991; Stone, 2000), but this choice does not affect our conclusions. We did not consider ^{10}Be ages that yielded results either significantly younger or older than the peak age of the moraine being dated. Discrimination of outliers from the main population of ages was based on visual inspection of probability age distribution plots, the 3-sigma rule, and the morpho-stratigraphic position of samples/ages on ice-derived landforms.

4. Results

4.1. Geomorphology

The geomorphic maps with the geochronological results and associated legends for El Toro, Las Arenas, El Viento, and El Despoblado valleys are presented in Figs. 3–7. Further detailed geomorphologic descriptions of these valleys can be found in Carraha et al. (2024).

4.1.1. Glacial features

The upper Limarí Basin includes outstanding erosional mountain glacial geomorphology carved in granitic rocks during Quaternary glaciations. This is best recognized by large-scale landforms including cirques, horns, arêtes, and U-shaped valleys, punctuated by tarn and mountain bogs ("*veranadas*"). Most of the cirques were exposed southward. Arêtes develop as sharp cirques and U-shaped valley edges, which can be tracked normally only for relatively short distances (c. 5–6 km). Most of these small valleys develop to the south and southwest and expose a relatively rapid change from steep to gentler valley sides. Glacial landforms (i.e., moraines) are ubiquitous within the formerly glaciated valleys of the Limarí Basin. Here, we describe, and ^{10}Be date, the outer two LIM I and LIM II moraines (see below), which for each

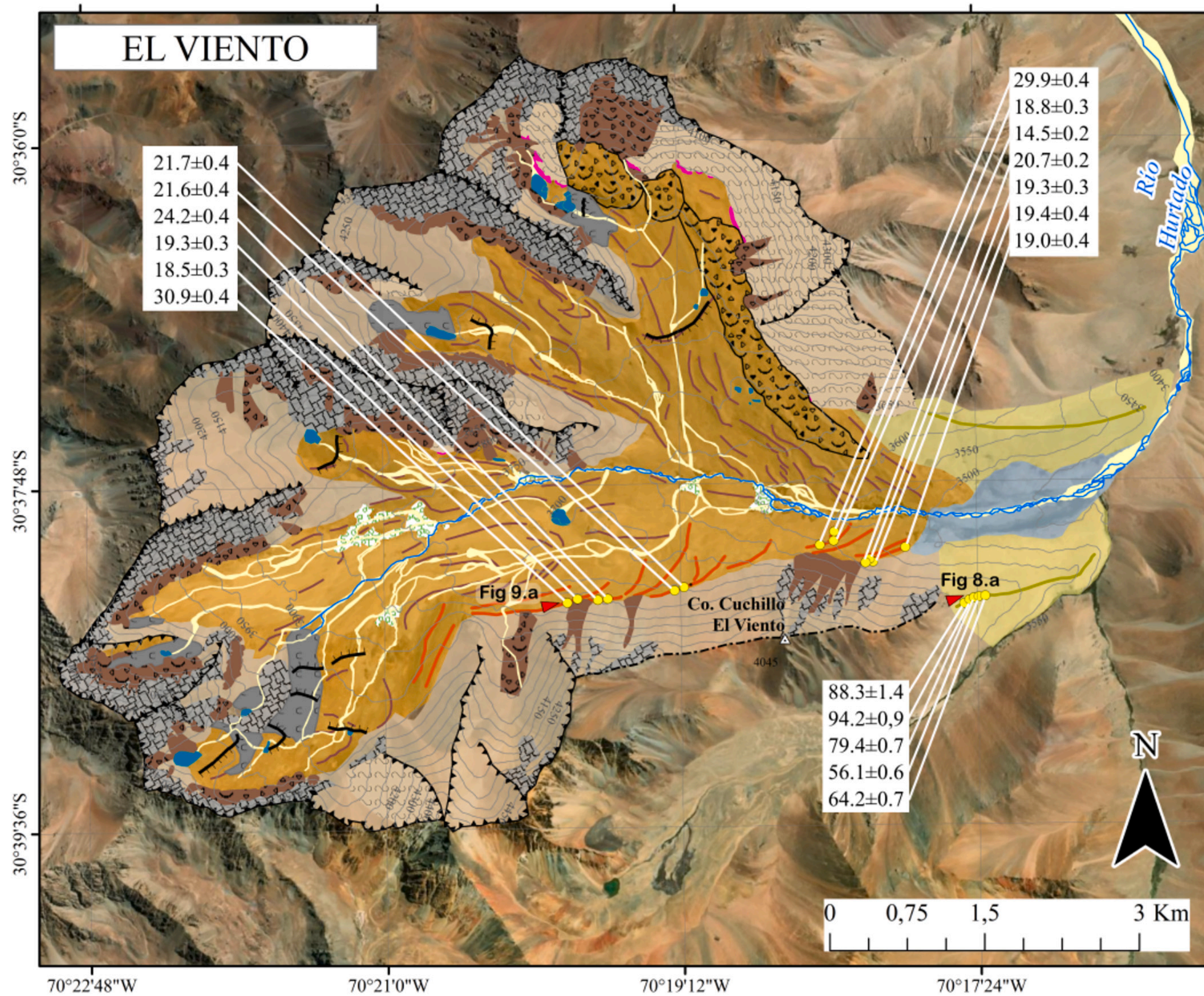

Fig. 5. ^{10}Be ages (in thousands of years ago; error 1 sigma) of rock samples from LIM I and LIM II moraines in the El Viento Valley, Andean highlands of the Río Limarí Basin. Base geomorphic map from Carraha et al. (2024). Red triangular arrows indicate the locations where photos were taken and the direction the camera was pointing.

singular valley are named using the local name, i.e., TOR I and TOR II (El Toro valley); LAR I and LAR II (Las Arenas valley); EV I and EV II (El Viento valley); and ED II (El Despoblado valley) (Carraha et al., 2024). All of these moraine belts were targeted for ^{10}Be dating. In El Despoblado, LIM I was deposited down-valley in El Ternero main valley and not included in our work. Other inboard (i.e., younger) and high-elevation moraine belts exist for the area as described in Carraha et al. (2024), in particular in the El Despoblado valley, where moraine arcs enclose cirques with headwalls reaching 5000 m a.s.l.

The LIM I landforms are preserved as conspicuous lateral moraines in all valleys, except for El Despoblado (Fig. 8). They stand-out as very wide features (more than hundred meters width, such as in El Viento or Las Arenas valleys). Moraines can extend over 2 km and occur at elevations between 2800 and 3600 m a.s.l. No obvious moraine deposits occur below this elevation down-valley. LIM I lateral moraine deposits occur about 6–10 km from the cirques (more extensive in the Hurtado sub-basin), marking near maximum extent of former ice, as inferred from their arcuate geometries towards the valley bottoms. Boulders on LIM I moraine may show significant weathering (e.g., in El Viento) if compared to the next inner moraine belt (LIM II). Boulders are subrounded and subangular indicating in some cases a subglacial origin (Fig. 8) (Boulton, 1978). LIM I moraine in Las Arenas can be very wide and flat in its up-valley section but narrow and steep in its lower part. The steepness of the moraine crests is higher where the landform is flanked by small river channels (Fig. 8). In some cases, the moraine LIM I was deposited over the valley flanks thus separating adjacent valleys, as in El Viento.

The inboard LIM II moraine can be tracked from the cirques to 3–8 km down-valley (more extensive in the Hurtado sub-basin). Most of the LIM II morainic relief occurs towards the valley sides where lateral moraine complexes define the sharp end of the landform (Fig. 9). Towards the valley bottoms, multiple lateral and latero-frontal ridges nested inside each other stand out from the moraine bouldery and hummocky surface. Thus, the valleys appear covered by moraine deposits from side to side describing a concave shape, with slopes angles of ~20–25° (Fig. 9), as in El Viento and El Despoblado. The proximal slope of the lateral moraine complexes exhibits a stepwise topography defined by the inboard ridges. Down-valley of El Toro, the lateral moraine complexes at both sides of the valley bottom acquire a lobate shape, with convex cross-sections. In general, the morainic bouldery surface has low relief (up to meters), although in some cases, topography can be more pronounced. For instance, at TOR II moraine the hummocky topography

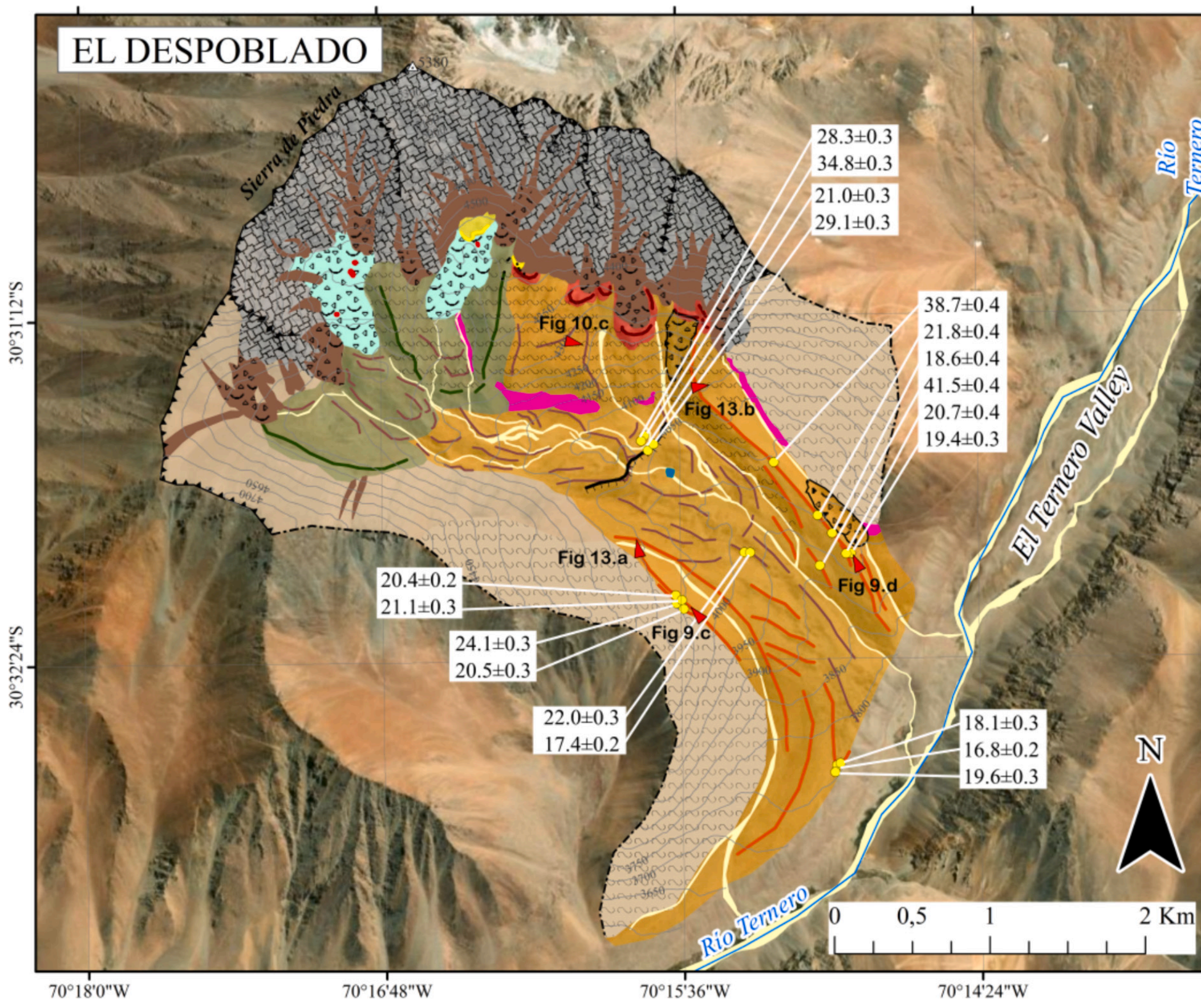

Fig. 6. ^{10}Be ages (in thousands of years ago; error 1 sigma) of rock samples from LIM II moraines in the El Despoblado Valley, Andean highlands of the Río Limarí Basin. Base geomorphic map from Carraha et al. (2024). Red triangular arrows indicate the locations where photos were taken and the direction the camera was pointing.

includes meso-landforms on its surface such as depressions probably evidencing former sinkholes (thermokarst structures; Kjær and Krüger (2001) and debris-filled fractures, resembling ground deformation by freeze-thaw action (Murton, 2021)) (Fig. 10). In El Toro, the LIM II moraine is flanked by steep ridges or margins, except in sections of the front where it can gently grade to the ground surface. In the El Despoblado valley, the right lateral former glacier margin occurs as lines of boulders deposited on the topography; the left lateral is a prominent moraine ridge (Fig. 9). In El Viento, either the slope talus grades towards the glacial till or a lateral moraine crest stands out over the valley side, in some cases separated by a terrace surface. In the first case, debris from both glacial and slope origins can be clearly distinguished in terms of shape, colour, and size. The LIM II extent is very well-defined in each of the studied valleys.

Both LIM I and LIM II moraines have bouldery surfaces. Boulders are of different sizes and degree of weathering (Figs. 8–12). Moraine boulders are rather subangular to subrounded, including even sides, denoting subglacial glacial erosion. Angular boulders are common as well, and can be associated with rock material sourced from the valley high walls (Boulton, 1978). LIM I boulders are significantly more weathered than LIM II boulders, this is particularly true for all valleys, except for Las Arenas. LIM I boulders in El Viento are the most weathered on the outer cm layer and show no signs of glacial striations. LIM I surface matrix consists of granular material. Surface of boulders in LIM II can appear striated when the outer mm layer is still preserved. Exfoliation of the surficial striated mm layer is post-depositional. Boulders in LIM I can also preserve striations.

4.1.2. *Periglacial features*

Periglacial landforms such as rock glaciers, gelifluction lobes, slope and protalus lobes were identified and described in detail in the study area by Carraha et al. (2024) (Fig. 13).

The periglacial landforms indicate the relevance of ground ice and permafrost occurrence. Their spatial setting in relation to the glacial features provides additional insight into the chronology of different climatic phases (Carraha et al., 2024). Periglacial landforms in our study area are more frequent above 3700 m a.s.l. and found mostly in association with cold south-facing slopes in the case of rock glaciers and south to southwestern aspects for other periglacial landforms. There is a greater dominance of periglacial landforms in the valleys of Río Hurtado sub-basin, where altitudes are higher, above about 4000 m a.s.l. Stripes filled with debris are identified in El Despoblado and El Toro valleys above 3500 m a.s.l. They manifest as sorted stripes, ranging from tens to hundreds of centimeters in length, and are sometimes filled with small rocks (around 5 cm diameter) and other times with larger rocks (around 20 cm diameter) (Carraha et al., 2024), similar to patterned ground representing the effects of cryoturbation (Trombotto, 2000). Meter-scale gelifluction lobes occur as protuberances on the flanks of detrital slopes ranging between 20 and 30°, but they are also frequent on moraine deposits, such as El Despoblado and El Toro LIM II moraines. Protalus

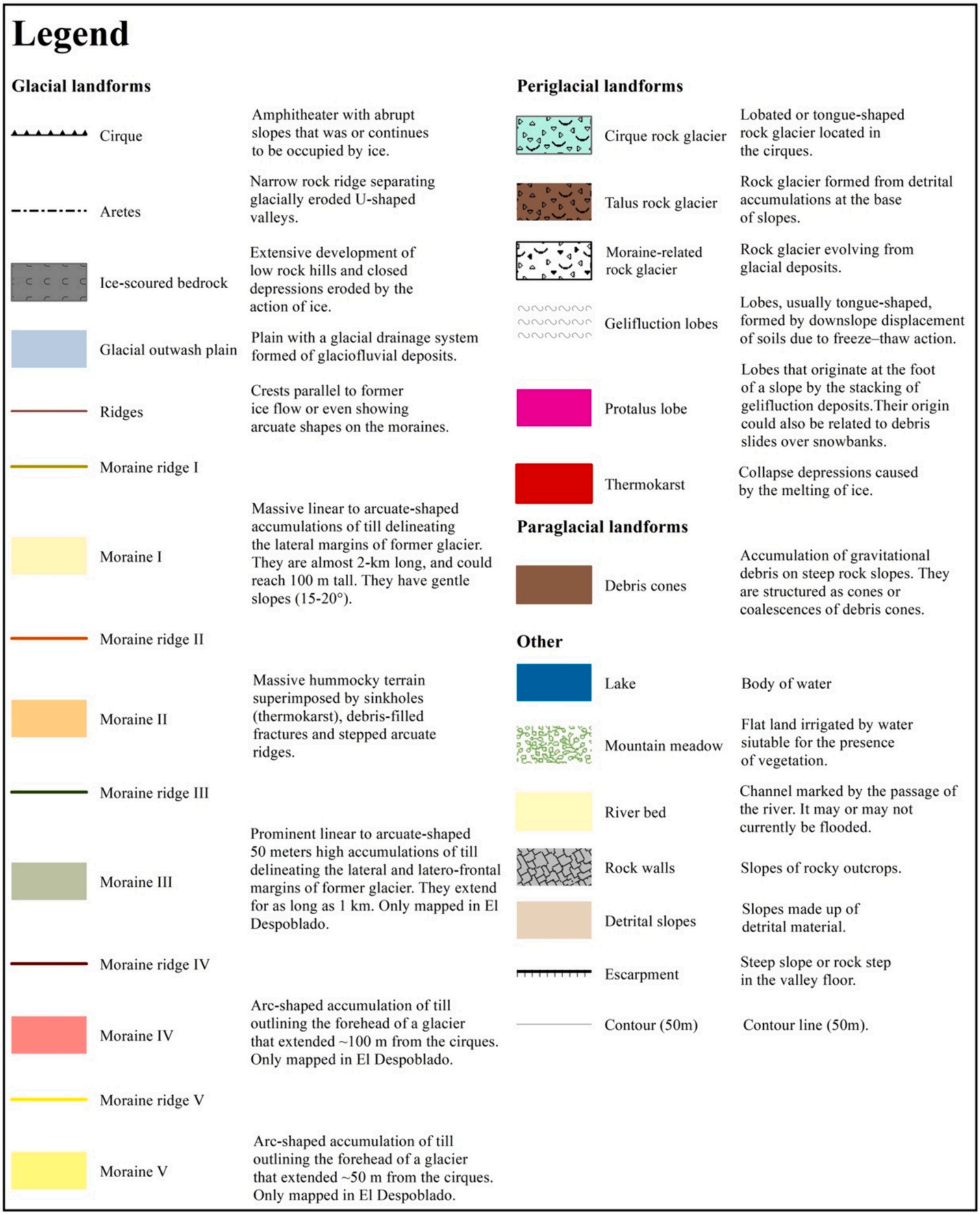

Fig. 7. Legend for geomorphic maps in Figs. 3–6.

lobes occur at the base of the gelifluction slopes where the slope changes from 25°–30° to ∼15°. Protalus lobes can develop laterally for hundreds of meters in most valleys (Figs. 3–6). They have flow structures characterized by ridges and furrows transversal to the flow direction. These landforms have also been referred to as protalus ramparts (Harrison et al., 2008) and their origin could also be related to debris slides over snowbanks. They could be considered as embryonic rock glaciers (Trombotto, 2000). Active and inactive rock glaciers, either occurring at the base of talus slopes, cirques or at the valley bottoms, are widespread in the El Despoblado and El Viento, but are less common in El Toro and

Table 1
Analytical data and attributes for the 74 new ^{10}Be samples at the El Viento, El Despoblado, El Toro, and Las Arenas valleys.[a]

CAMS Lab ID	Sample Lab ID	Lat °S	Long °W	Elevation (m a.s.l.)	Sample thickness (cm)	Boulder height (cm)	Shielding correction	Quartz weight (g)	^{9}Be (μg)	^{10}Be ± 1σ (10^4 atoms g^{-1})	$^{10}Be/^{9}Be$ ratio ± 1σ ($\times 10^{-13}$)	^{10}Be standardization
El Viento Moraine I												
BE51526	LICUCBe3-EV2201	−30.6407	−70.2913	3621	2.9	50	0.996	23.07	244	326 ± 5	44.6 ± 0.7	07KNSTD
BE51527	LICUCBe4-EV2202	−30.6406	−70.2911	3615	2.4	50	0.996	14.10	245	351 ± 3	29.2 ± 0.3	07KNSTD
BE51528	LICUCBe5-EV2203	−30.6403	−70.2905	3613	2.8	40	0.996	15.71	243	293 ± 3	27.3 ± 0.2	07KNSTD
BE51529	LICUCBe6-EV2204	−30.6402	−70.2904	3609	2.3	50	0.997	14.51	245	204 ± 2	17.5 ± 0.2	07KNSTD
BE51530	LICUCBe7-EV2205	−30.6401	−70.2894	3601	2.5	60	0.997	11.65	243	235 ± 3	16.3 ± 0.2	07KNSTD
El Viento Moraine II												
BE52762	LICUCBe6-EV2206	−30.6402	−70.3314	3787	2.7	70	0.988	22.24	244	125 ± 2	16.6 ± 0.2	07KNSTD
BE52763	LICUCBe7-EV2207	−30.6401	−70.3306	3785	2.2	70	0.988	22.67	244	70 ± 1	9.48 ± 0.12	07KNSTD
BE52764	LICUCBe8-EV2208	−30.6401	−70.3284	3768	1.8	80	0.987	22.00	243	74 ± 1	9.62 ± 0.17	07KNSTD
BE52765	LICUCBe9-EV2209	−30.6400	−70.3275	3769	2.5	60	0.986	22.22	243	95 ± 2	12.6 ± 0.2	07KNSTD
BE51655	LICUCBe3-EV2210	−30.6389	−70.3209	3720	1.6	90	0.990	15.42	246	82 ± 1	7.48 ± 0.13	07KNSTD
BE51656	LICUCBe3-EV2211	−30.6387	−70.3197	3727	2.2	80	0.989	16.32	247	82 ± 2	7.90 ± 0.16	07KNSTD
BE51657	LICUCBe5-EV2213	−30.6357	−70.2972	3498	2.4	130	0.988	15.04	247	62 ± 1	5.50 ± 0.10	07KNSTD
BE51523	LICUCBe1-EV2214	−30.6371	−70.3005	3546	1.7	80	0.985	21.15	246	66 ± 1	8.20 ± 0.15	07KNSTD
BE51524	LICUCBe2-EV2215	−30.6368	−70.3010	3543	3.0	150	0.984	21.64	245	64 ± 1	8.21 ± 0.14	07KNSTD
BE52766	LICUCBe10-EV2216	−30.6372	−70.3013	3556	1.8	100	0.977	22.12	246	71 ± 1	9.18 ± 0.13	07KNSTD
BE52767	LICUCBe11-EV2217	−30.6343	−70.3044	3536	1.6	130	0.991	23.76	244	63 ± 1	8.91 ± 0.12	07KNSTD
BE52768	LICUCBe12-EV2218	−30.6355	−70.3055	3574	2.5	50	0.988	22.16	242	109 ± 1	14.4 ± 0.2	07KNSTD
BE52769	LICUCBe13-EV2219	−30.6355	−70.3044	3566	2.5	50	0.989	22.04	243	47 ± 1	6.23 ± 0.11	07KNSTD
El Despoblado Moraine II												
BE52741	LICUCBe1-ES2201	−30.5327	−70.2497	3958	2.3	70	0.994	22.49	246	78 ± 2	10.3 ± 0.2	07KNSTD
BE52742	LICUCBe2-ES2202	−30.5339	−70.2485	3940	2.6	110	0.995	22.32	246	81 ± 1	10.6 ± 0.1	07KNSTD
BE52743	LICUCBe3-ES2203	−30.5339	−70.2489	3939	1.9	70	0.995	22.18	248	87 ± 2	11.3 ± 0.2	07KNSTD
BE52744	LICUCBe4-ES2204	−30.5318	−70.2507	3980	2.8	130	0.993	22.23	243	94 ± 2	12.5 ± 0.2	07KNSTD
BE52745	LICUCBe5-ES2205	−30.5286	−70.2537	4019	1.9	50	0.990	22.20	245	177 ± 2	23.2 ± 0.2	07KNSTD
BE52746	LICUCBe6-ES2206	−30.5346	−70.2508	3900	2.2	120	0.993	22.33	244	184 ± 2	24.3 ± 0.2	07KNSTD
BE52748	LICUCBe7-ES2207	−30.5367	−70.2603	4027	2.0	110	0.994	22.47	245	109 ± 2	14.5 ± 0.2	07KNSTD
BE52749	LICUCBe8-ES2208	−30.5365	−70.2602	4024	2.2	100	0.993	22.32	245	89 ± 1	11.8 ± 0.1	07KNSTD
BE52750	LICUCBe9-ES2209	−30.5366	−70.2600	4025	2.0	100	0.993	22.38	245	93 ± 1	12.3 ± 0.2	07KNSTD
BE52751	LICUCBe10-ES2210	−30.5370	−70.2598	4021	1.4	80	0.993	22.57	245	90 ± 1	12.0 ± 0.2	07KNSTD
BE52752	LICUCBe11-ES2211	−30.5462	−70.2495	3731	2.7	170	0.995	24.54	246	67 ± 1	9.66 ± 0.16	07KNSTD
BE52753	LICUCBe12-ES2212	−30.5461	−70.2494	3729	2.2	90	0.994	22.36	247	62 ± 1	8.06 ± 0.11	07KNSTD
BE52754	LICUCBe13-ES2213	−30.5466	−70.2497	3728	1.7	160	0.994	22.69	246	160 ± 1	9.83 ± 0.14	07KNSTD
BE53737	LICUCBe11-ES2214	−30.5271	−70.2627	4044	1.6	140	0.982	26.49	245	74 ± 1	25.0 ± 0.2	07KNSTD

(*continued on next page*)

Table 1 (*continued*)

CAMS Lab ID	Sample Lab ID	Lat °S	Long °W	Elevation (m a.s.l.)	Sample thickness (cm)	Boulder height (cm)	Shielding correction	Quartz weight (g)	^{9}Be (μg)	^{10}Be ± 1σ (10^4 atoms g^{-1})	$^{10}Be/^{9}Be$ ratio ± 1σ ($\times10^{-13}$)	^{10}Be standardization
BE52756	LICUCBe1-ES2215	−30.5271	−70.2629	4044	1.9	90	0.985	21.53	247	130 ± 1	16.4 ± 0.2	07KNSTD
BE52757	LICUCBe2-ES2216	−30.5275	−70.2619	4024	2.4	110	0.986	22.25	246	133 ± 2	17.4 ± 0.2	07KNSTD
BE52758	LICUCBe3-ES2217	−30.5276	−70.2617	4029	2.8	90	0.982	23.11	247	91 ± 1	12.4 ± 0.2	07KNSTD
BE52759	LICUCBe4-ES2218	−30.5338	−70.2556	3958	2.2	100	0.992	22.19	245	95 ± 1	12.4 ± 0.1	07KNSTD
BE52760	LICUCBe5-ES2219	−30.5338	−70.2555	3934	2.4	110	0.992	23.62	244	71 ± 1	9.98 ± 0.13	07KNSTD
El Toro Moraine I												
BE51534	LICUCBe11-TOR2020	−31.3031	−70.7847	3165	1.4	120	0.998	12.36	243	213 ± 3	15.7 ± 0.2	07KNSTD
BE51659	LICUCBe6-TOR2021	−31.3032	−70.7851	3158	1.4	60	0.998	8.34	247	126 ± 2	6.20 ± 0.09	07KNSTD
BE51533	LICUCBe10-TOR2022	−31.3030	−70.7839	3171	1.9	100	0.998	11.26	244	150 ± 2	10.0 ± 0.1	07KNSTD
BE51532	LICUCBe9-TOR2023	−31.3038	−70.7800	3241	1.3	70	0.998	10.09	242	123 ± 2	7.45 ± 0.15	07KNSTD
BE51531	LICUCBe8-TOR2024	−31.3038	−70.7801	3242	1.9	80	0.998	10.45	244	109 ± 1	6.60 ± 0.09	07KNSTD
El Toro Moraine II												
BE53726	LICUCBe1-TOR2001	−31.2896	−70.7415	3618	2.2	130	0.989	60.55	247	174 ± 1	61.9 ± 0.5	07KNSTD
BE53727	LICUCBe2-TOR2002	−31.2887	−70.7419	3609	1.7	110	0.988	65.57	246	70 ± 1	27.2 ± 0.2	07KNSTD
BE53728	LICUC-Be3-TOR2003	−31.2884	−70.7426	3612	2.3	120	0.989	57.03	246	65 ± 1	21.6 ± 0.2	07KNSTD
BE53729	LICUCBe4-TOR2004	−31.2884	−70.7426	3614	1.8	250	0.987	53.91	245	63 ± 1	19.9 ± 0.2	07KNSTD
BE53731	LICUCBe5-TOR2005	−31.2922	−70.7441	3579	1.5	100	0.988	24.85	245	330 ± 2	48.8 ± 0.4	07KNSTD
BE53732	LICUCBe6-TOR2006	−31.2936	−70.7475	3568	1.1	140	0.991	17.14	245	74 ± 1	7.51 ± 0.08	07KNSTD
BE53733	LICUCBe7-TOR2007	−31.2941	−70.7522	3557	2.3	110	0.996	32.63	246	113 ± 1	21.7 ± 0.2	07KNSTD
BE53734	LICUCBe8-TOR2008	−31.2921	−70.7550	3561	2.1	70	0.998	23.11	246	77 ± 1	10.5 ± 0.2	07KNSTD
BE53735	LICUCBe9-TOR2009	−31.2922	−70.7549	3565	1.9	80	0.997	26.71	245	211 ± 2	33.3 ± 0.3	07KNSTD
BE53736	LICUCBe10-TOR2010	−31.2921	−70.7550	3567	1.9	100	0.997	24.61	244	88 ± 1	12.9 ± 0.1	07KNSTD
BE52466	LICUCBe1-TOR2011	−31.2864	−70.7562	3553	1.9	120	0.994	17.30	246	74 ± 1	7.53 ± 0.14	07KNSTD
BE52467	LICUCBe2-TOR2012	−31.2871	−70.7575	3548	2.2	160	0.997	20.63	242	74 ± 1	9.10 ± 0.17	07KNSTD
BE52468	LICUCBe3-TOR2013	−31.2893	−70.7692	3419	1.8	150	0.998	15.41	246	45 ± 1	4.12 ± 0.09	07KNSTD
BE52469	LICUCBe3-TOR2014	−31.2892	−70.7691	3442	1.7	70	0.998	15.13	246	31 ± 1	2.73 ± 0.05	07KNSTD
BE52470	LICUCBe5-TOR2015	−31.2903	−70.7712	3393	1.6	90	0.996	15.62	244	43 ± 1	3.97 ± 0.07	07KNSTD
BE52471	LICUCBe6-TOR2016	−31.2909	−70.7723	3371	1.7	80	0.994	17.33	245	48 ± 1	4.93 ± 0.09	07KNSTD
BE52473	LICUCBe7-TOR2017	−31.2911	−70.7727	3367	1.7	120	0.994	17.69	246	41 ± 1	4.30 ± 0.07	07KNSTD
BE51653	LICUCBe1-TOR2018	−31.2920	−70.7714	3347	1.6	140	0.996	14.21	248	56 ± 1	4.62 ± 0.09	07KNSTD
BE51654	LICUCBe2-TOR2019	−31.2929	−70.7721	3346	2.6	80	0.997	16.06	246	59 ± 1	5.59 ± 0.10	07KNSTD
Las Arenas Moraine I												
BE51660	LICUCBe7-LAR2001	−31.3529	−70.8140	3347	1.2	70	0.999	8.26	247	190 ± 3	9.18 ± 0.14	07KNSTD
BE51535	LICUCBe12-LAR2002	−31.3523	−70.8147	3338	2.1	70	0.999	10.10	244	450 ± 5	26.9 ± 0.3	07KNSTD
BE51661	LICUCBe8-LAR2003	−31.3512	−70.8183	3315	1.4	70	0.999	8.14	246	214 ± 3	10.2 ± 0.2	07KNSTD

(*continued on next page*)

Table 1 (*continued*)

CAMS Lab ID	Sample Lab ID	Lat °S	Long °W	Elevation (m a.s.l.)	Sample thickness (cm)	Boulder height (cm)	Shielding correction	Quartz weight (g)	^{9}Be (μg)	^{10}Be ± 1σ (10^4 atoms g^{-1})	^{10}Be/^{9}Be ratio ± 1σ ($\times10^{-13}$)	^{10}Be standardization
BE51662	LICUCBe9-LAR2004	−31.3509	−70.8218	3295	2.0	70	0.999	5.55	245	148 ± 3	4.84 ± 0.09	07KNSTD
BE51663	LICUCBe10-LAR2005	−31.3516	−70.8244	3255	1.4	60	0.999	8.25	246	78 ± 1	3.80 ± 0.07	07KNSTD
BE51664	LICUCBe11-LAR2006	−31.3502	−70.8303	3137	1.0	110	0.998	6.84	245	90 ± 2	3.62 ± 0.07	07KNSTD
BE51665	LICUCBe12-LAR2007	−31.3502	−70.8302	3142	1.9	80	0.998	8.23	246	190 ± 4	9.21 ± 0.17	07KNSTD
BE51666	LICUCBe13-LAR2008	−31.3503	−70.8296	3152	1.7	80	0.998	7.97	246	75 ± 1	3.51 ± 0.06	07KNSTD
Las Arenas Moraine II												
BE52474	LICUCBe8-LAR2009	−31.3498	−70.8055	3347	2.0	70	0.998	11.90	244	73 ± 1	5.16 ± 0.08	07KNSTD
BE52475	LICUCBe9-LAR2010	−31.3509	−70.8042	3369	2.7	100	0.998	20.69	241	63 ± 1	7.87 ± 0.11	07KNSTD
BE52476	LICUCBe10-LAR2011	−31.3512	−70.8043	3370	1.8	60	0.997	15.34	243	60 ± 1	5.47 ± 0.09	07KNSTD
BE52477	LICUCBe11-LAR2012	−31.3512	−70.8040	3372	2.9	120	0.998	15.51	243	60 ± 1	5.58 ± 0.11	07KNSTD
BE52478	LICUCBe12-LAR2013	−31.3505	−70.8047	3363	2.0	60	0.998	17.62	246	59 ± 1	6.16 ± 0.09	07KNSTD

Blanks

CAMS Lab ID	Sample Lab ID	Lat °S	Long °W	Elevation (m a.s.l.)	Sample thickness (cm)	Boulder height (cm)	Shielding correction	Quartz weight (g)	^{9}Be (μg)	^{10}Be ± 1σ (10^4 atoms g^{-1})	^{10}Be/^{9}Be ratio ± 1σ ($\times10^{-16}$)	^{10}Be standardization
BE51522	LICUCBlank1								246		6.80 ± 1	07KNSTD
BE51525	LICUCBlank2								244		4.98 ± 0.9	07KNSTD
BE51652	LICUCBlank3								244		6.13 ± 1	07KNSTD
BE51658	LICUCBlank4								245		8.45 ± 2	07KNSTD
BE52465	LICUCBlank5								248		6.60 ± 1	07KNSTD
BE52472	LICUCBlank6								247		7.61 ± 1	07KNSTD
BE52740	LICUCBlank7								246		6.98 ± 1	07KNSTD
BE52747	LICUCBlank8								245		15.0 ± 2	07KNSTD
BE52755	LICUCBlank9								246		22.3 ± 3	07KNSTD
BE52761	LICUCBlank10								244		9.92 ± 1	07KNSTD
BE53725	LICUCBlank11								246		7.68 ± 1	07KNSTD
BE53730	LICUCBlank12								245		11.6 ± 2	07KNSTD

[a] Samples were measured with a homemade (pk18D2) ^{9}Be carrier concentration of 966 ± 36 ppm. Samples in the lab were processed in six different batches of 12–13 samples including two blanks each. The ^{10}Be/^{9}Be measured for all blanks (n = 12) ranged between 4,9818E-16 and 2,2321E-15. ^{10}Be concentrations in samples have been corrected for background ^{10}Be atoms detected in procedural blanks. For this correction we used the mean of the two respective procedural blank ratios ^{10}Be/^{9}Be of each batch of samples. Reported ^{10}Be/^{9}Be value for 07KNSTD is 2.85E-12 (Nishiizumi et al., 2007).

Las Arenas (Figs. 3–6). Talus rock glaciers have steep fronts >10 m in height and lengths up to 200 m. One distinct talus rock glacier in El Toro develops from the valley slope until the right LIM II lateral ridge, and is made-up by distinct local angular debris (Fig. 3). This rock glacier has a rather subdued surface geomorphology and appears to be inactive. In El Viento, an interpreted rock glacier occurs adjacent to the LIM II hummocky moraine extending along the main valley for near 2 km (Fig. 5). Another valley rock glacier develops along the Las Arenas valley from near the cirque until 2 km down-valley. In the El Toro and El Despoblado valleys, gelifluction lobes and rock glaciers appear overprinting the LIM II hummocky moraine, particularly where high-slope angles favored creep of perennially frozen ice-rich materials. In some cases, creeping lobes appear superimposed to each other. Distinct furrows and ridges structures on LIM II moraine in El Toro occur after topographic steps, and denote rock glacier viscous flow of moraine deposits. In the same valley, near the cirques, lateral moraines display viscous flow structures on their ~30° proximal slopes (Fig. 14). The mapped active rock glaciers near the headwalls above 3600 m a.s.l. in the southern part of the Limarí Basin (Combarbalá) and above 3900 m a.s.l. to the north (Río Hurtado) indicate present-day ice-rich permafrost creep (Fig. 15) (Carraha et al., 2024).

4.2. Geochronology

^{10}Be data is presented after rejecting outliers (see Materials and methods section) and detailed in Tables 1 and 2.

4.2.1. LIM I moraine

Dates from LIM I were obtained in El Toro, Las Arenas, and El Viento, yielding dissimilar ages in these valleys (Figs. 3–5; Table 2). In El Toro, LIM I ages range between 41.2 ± 0.6 and 35.0 ± 0.5 ka (n = 3). LIM I ages in the Las Arenas valley range between 65.3 ± 1.0 and 24.9 ± 0.5 ka (n = 7). LIM I ages in the El Viento valley range between 94.2 ± 0.9 and 56.0 ± 0.6 ka (n = 5).

4.2.2. LIM II moraine

From El Toro II moraine a total of 19 rock samples were obtained from different sections of the hummocky moraine, including two tributary valleys: the right and left lateral ridges, areas of accumulation of boulders, and ridges on top of topographic thresholds by the El Toro

Table 2

^{10}Be exposure cosmogenic ages for LIM I and LIM II moraines in El Viento, El Despoblado, El Toro, and Las Arenas valleys.[a]

Sample ID	St	Lm	LSDn
El Viento Moraine I			
EV2201	96,700 ± 1500	**88,300 ± 1400**	87,400 ± 1300
EV2202	104,000 ± 1000	**94,200 ± 900**	93,300 ± 900
EV2203	86,800 ± 800	**79,400 ± 700**	78,300 ± 700
EV2204	59,900 ± 700	**56,100 ± 600**	55,300 ± 600
EV2205	69,800 ± 800	**64,200 ± 700**	63,400 ± 700
El Viento Moraine II			
EV2206	*33,700 ± 500*	***30,900 ± 400***	*30,300 ± 400*
EV2207	18,800 ± 300	**18,500 ± 300**	18,500 ± 300
EV2208	19,800 ± 300	**19,300 ± 300**	19,300 ± 300
EV2209	25,800 ± 500	**24,200 ± 400**	23,900 ± 400
EV2210	22,700 ± 400	**21,600 ± 400**	21,500 ± 400
EV2211	22,700 ± 500	**21,700 ± 400**	21,600 ± 400
EV2213	19,400 ± 400	**19,000 ± 400**	19,100 ± 400
EV2214	19,900 ± 400	**19,400 ± 400**	19,500 ± 400
EV2215	19,800 ± 300	**19,300 ± 300**	19,400 ± 300
EV2216	21,500 ± 300	**20,700 ± 200**	20,800 ± 250
EV2217	19,100 ± 300	**18,800 ± 300**	18,900 ± 300
EV2218	*32,700 ± 400*	***29,900 ± 400***	*29,700 ± 400*
EV2219	*14,300 ± 200*	***14,500 ± 200***	*14,500 ± 200*
El Despoblado Moraine II			
ES2201	19,000 ± 400	**18,600 ± 400**	18,500 ± 400
ES2202	19,900 ± 300	**19,400 ± 300**	19,300 ± 300
ES2203	21,400 ± 400	**20,700 ± 400**	20,600 ± 400
ES2204	22,900 ± 400	**21,800 ± 400**	21,600 ± 400
ES2205	*42,100 ± 400*	***38,700 ± 400***	*37,900 ± 400*
ES2206	*46,400 ± 500*	***41,500 ± 400***	*40,700 ± 400*
ES2207	25,700 ± 400	**24,100 ± 300**	23,600 ± 300
ES2208	21,000 ± 300	**20,400 ± 200**	20,200 ± 200
ES2209	21,900 ± 300	**21,100 ± 300**	20,800 ± 300
ES2210	21,100 ± 300	**20,500 ± 300**	20,300 ± 300
ES2211	18,400 ± 300	**18,100 ± 300**	18,100 ± 300
ES2212	16,900 ± 200	**16,800 ± 200**	16,800 ± 200
ES2213	20,200 ± 300	**19,600 ± 300**	19,600 ± 200
ES2214	*37,700 ± 300*	***34,800 ± 300***	*34,200 ± 300*
ES2215	*30,700 ± 300*	***28,300 ± 300***	*27,600 ± 300*
ES2216	*31,700 ± 400*	***29,100 ± 300***	*28,400 ± 300*
ES2217	21,900 ± 300	**21,000 ± 300**	20,800 ± 300
ES2218	23,100 ± 300	**22,000 ± 300**	21,700 ± 300
ES2219	17,600 ± 200	**17,400 ± 200**	17,300 ± 200
El Toro Moraine I			
TOR2020	*77,600 ± 1100*	***71,100 ± 1000***	*70,800 ± 1000*
TOR2021	45,700 ± 700	**41,200 ± 600**	41,100 ± 600
TOR2022	54,300 ± 800	**49,800 ± 700**	49,500 ± 700
TOR2023	42,600 ± 900	**39,100 ± 800**	39,100 ± 800
TOR2024	37,800 ± 500	**35,000 ± 500**	35,000 ± 500
El Toro Moraine II			
TOR2001	*49,800 ± 400*	***44,600 ± 400***	*43,300 ± 300*
TOR2002	20,000 ± 200	**19,500 ± 200**	19,500 ± 200
TOR2003	18,400 ± 200	**18,100 ± 200**	18,100 ± 200
TOR2004	17,800 ± 200	**17,600 ± 200**	17,600 ± 200
TOR2005	*97,900 ± 700*	***89,600 ± 700***	*88,500 ± 700*
TOR2006	21,400 ± 200	**20,700 ± 200**	20,700 ± 200
TOR2007	*33,100 ± 300*	***30,400 ± 300***	*30,000 ± 300*
TOR2008	22,300 ± 300	**21,400 ± 300**	21,300 ± 300
TOR2009	*61,600 ± 500*	***57,800 ± 500***	*57,000 ± 500*
TOR2010	25,500 ± 200	**24,000 ± 200**	23,700 ± 200
TOR2011	21,600 ± 400	**20,800 ± 400**	20,800 ± 400
TOR2012	21,600 ± 400	**20,900 ± 400**	20,800 ± 400
TOR2013	14,100 ± 300	**14,300 ± 300**	14,400 ± 300
TOR2014	*9400 ± 200*	***10,200 ± 200***	*10,400 ± 200*
TOR2015	13,500 ± 300	**13,800 ± 300**	13,900 ± 300
TOR2016	15,500 ± 300	**15,500 ± 300**	15,600 ± 300
TOR2017	13,300 ± 200	**13,600 ± 200**	13,800 ± 200
TOR2018	18,100 ± 300	**17,800 ± 300**	18,000 ± 300
TOR2019	19,400 ± 400	**19,000 ± 400**	19,200 ± 400
Las Arenas Moraine I			
LAR2001	61,700 ± 1000	**57,900 ± 900**	57,600 ± 900
LAR2002	*151,600 ± 1600*	***131,700 ± 1400***	*128,200 ± 1300*
LAR2003	71,100 ± 1100	**65,300 ± 1000**	64,700 ± 1000
LAR2004	49,700 ± 900	**44,500 ± 800**	43,900 ± 800
LAR2005	26,600 ± 500	**24,900 ± 500**	24,800 ± 500
LAR2006	32,600 ± 600	**30,000 ± 600**	30,000 ± 600
LAR2007	70,200 ± 1400	**64,600 ± 1200**	64,500 ± 1200
LAR2008	27,100 ± 400	**25,300 ± 400**	25,400 ± 400
Las Arenas Moraine II			
LAR2009	23,700 ± 400	**22,500 ± 400**	22,400 ± 400
LAR2010	20,500 ± 300	**19,900 ± 300**	20,000 ± 300
LAR2011	19,200 ± 300	**18,800 ± 300**	19,000 ± 300
LAR2012	19,500 ± 400	**19,100 ± 400**	19,200 ± 400
LAR2013	19,100 ± 300	**18,700 ± 300**	18,900 ± 300

[a] ^{10}Be ages ± internal or analytical error (1 s, AMS) in years calculated with three different scaling protocols as reported by the online age calculator (version 3, Balco et al., 2008). "St" is the is dependent scaling scheme of Stone (2000); "Lm" is the time dependent version of Stone/Lal scaling scheme (Lal, 1991; Stone, 2000); LSDn is the time dependent version of Lifton et al. (2014) scaling scheme. We discuss the "Lm" age output in our paper (bold text). All ages were calculated using a ^{10}Be production rate of 3.71 ± 0.11 atoms g^{-1} yr^{-1} measured at south Andes (Kaplan et al., 2011). Density of rock used for calculating ^{10}Be ages is 2.65 g cm^{-3}. Outliers have been italicized.

Lake and by the cirque. The ages from the outermost right lateral ridge range between 15.5 ± 0.3 and 10.2 ± 0.2 ka (n = 5). These ages cluster between 15.5 ± 0.3 and 13.6 ± 0.3 ka (n = 4), hence the youngest age is rejected as an outlier. We note this age range is significantly younger than the other LIM II ages obtained from the other three valleys, with implications we discuss further down (Section 5.4.3). Two samples a few tens of meters inboard of the right lateral yielded an age range between 19.0 ± 0.4 and 17.8 ± 0.3 ka, which is slightly younger than the ages from two samples obtained from boulders resting in the outermost left lateral moraine ridge up-valley both yielding an identical age of 20.8 ± 0.4 ka (n = 2). Three boulders by the lake El Toro obtained from boulders perched on bedrock, standing on a ridge and on the hummocky moraine yielded a range between 23.9 ± 0.2 and 20.7 ± 0.2 ka. Finally, three boulders few hundred meters from the cirque headwall yielded an age range between 19.5 ± 0.2 and 17.6 ± 0.2 ka.

In the Las Arenas valley, LIM II moraine was dated with five boulders resting on ridges near the distal position of this landform. Boulders yielded an age range between 22.5 ± 0.4 and 18.7 ± 0.3 ka (n = 5).

In the El Viento valley, the LIM II moraine was dated based on 13 boulders resting on outer and inboard right lateral moraine ridges. Some of the dated boulders were located in stable positions at the transition zone between scree talus slopes and moraine ridges thus delineating the outermost position of the former glacier (Fig. 12). The boulders yielded an age range for moraine formation between 24.2 ± 0.4 and 18.5 ± 0.3 ka (n = 10).

In the El Despoblado valley, the LIM II moraine was dated based on 19 ^{10}Be ages from the outer and inner sections of this landform. Four samples forming part of discrete lines of boulders demarking precisely former maximum positions of the glacier in this valley yielded an age range between 24.1 ± 0.3 and 20.4 ± 0.2 ka (n = 4). Four boulders sampled from the left outermost lateral crest yielded an age range between 21.8 ± 0.4 and 18.6 ± 0.4 ka (n = 4). Three boulders from the outer crest merging the El Ternero right lateral yielded an age range of 19.6 ± 0.3 - 16.8 ± 0.3 ka (n = 3). Inboard ridges near the center of LIM II in El Despoblado valley yielded ages between 22.0 ± 0.3 – 17.4 ± 0.2 ka (n = 2). Two nearby inboard ridges yielded ages ranging between 34.8 ± 0.3 – 21.0 ± 0.3 ka (n = 4). Another boulder resting on an inboard ridge yielded an age of 41.5 ± 0.4 ka. Because these inboard ridges cannot be older than the outer ridges, we exclude the samples

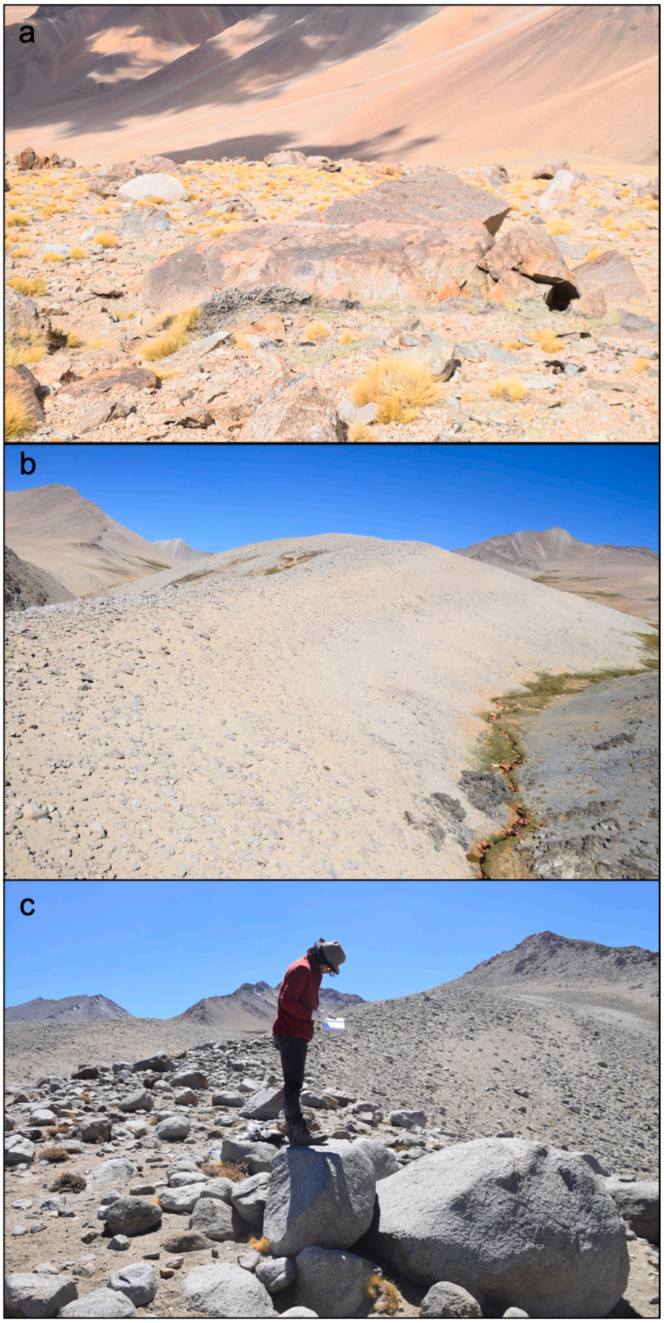

Fig. 8. The LIM I moraine landform in each of the studied valleys: El Viento (a), Las Arenas (b) and El Toro (c).

>28 ka (n = 4) when estimating the El Despoblado II moraine age, which yielded an age range between 17.4 ± 0.2 and 24.1 ± 0.3 ka. As in the other valleys, all rejected outliers are significantly older (or younger) than the main population of dates, and not included to constrain the age of the LIM II landform (Fig. 16). Nonetheless, we discuss the implications of the whole population of dates in the next section.

5. Discussion

5.1. Landform interpretation

Interpretation of massive and diamictic landforms can be problematic in this part of the Andes where mass-wasting deposits may have morphologic similarities with moraine deposits or vice versa (Paskoff, 1977; Abele, 1984; Antinao and Gosse, 2009; Moreiras et al., 2015). Both glacial and gravitational types of deposits can result in a massive chaotic and irregular landform (Abele, 1984). Nonetheless, several lines of evidence can be used for safe interpretation and accurate identification of landform evolution (Abele, 1984; Charrier et al., 2019). In this work, LIM I and LIM II landforms have been interpreted to be products of glacial origin based on their (1) ridged geometry, (2) presence on both sides of the valleys denoting lateral moraine complexes deposited at the margins of former glaciers, (3) occurrence on the topographic divide of contiguous valleys with no possible gravitational origin (LIM I), and (4) the presence of subglacially shaped clasts, in some cases including distinct signs of glacial abrasion (i.e., striations, Fig. 11). Thus, LIM I and LIM II moraine belts represent two distinct phases of glacial advances. On the one hand, LIM I has been preserved as prominent lateral moraines in all valleys with granitoid boulders covering its surface, represent the main ice advance in the study area. This glacial advance reached near 6–10 km in extent and was the most extensive. The size of the lateral moraines may indicate more than a single glacial expansion into the same extent (Benn and Owen, 2002). On the other hand, the inboard LIM II moraine is preserved as a massive lateral moraine complex. A cross-section describes a concave geometry between both valley sides with massive hummocky debris accumulation increasing towards the slopes demarking the LIM II glacial extent. LIM II represents a less extensive glacier advance than LIM I, reaching 3–8 km from the cirques and embracing a main second phase of ice expansion in the study area.

5.2. Moraines from debris-covered glaciers

In this section, we discuss evidence for former debris-covered glaciers occupying the studied valleys. As discussed below, we interpret the LIM II moraine as a main advance that was followed by the steady retreat of a debris-covered glacier. A sequence of inboard ridges was built in response to multiple cycles of glacier re-advance and retreat during overall deglaciation into the cirques and final glacier collapse.

Despite we did not provide absolute data regarding the shape of the boulders on LIM II moraine, our field observations indicate frequent subangular to subrounded boulder shapes, which help to discriminate how the debris was entrained and transported (Boulton, 1978; Anderson, 2000). Angular to subangular boulders are linked to a high-level supraglacial passive transport (Boulton, 1978). These boulders are delivered to the glacier surface from the surrounding steep valley slopes by gravity processes (e.g., rock fall and avalanche debris) affecting physically weathered bedrock and available slope sediments (Benn and Owen, 2002). On the other hand, boulders with smooth sides and subrounded shapes, in some cases preserving striations, indicate a subglacial active transport along the traction zone (Boulton, 1978). These glacially polished boulders could have been eroded away by plucking at the glacier sole or alternatively, delivered from the headwalls in the glacier accumulation area where they became buried under snow and ice eventually reaching the traction basal zone (Boulton, 1978). The presence of basal boulders on the LIM moraines surface requires subglacial debris being elevated to the supraglacial by basal freeze-on processes, along thrust planes in polythermal glaciers, or planes separating active and inactive glacier marginal zones (Hambrey et al., 1999; Benn and Owen, 2002). Finding of basal boulders in lateral moraine complexes, such as LIM II, is rather expected, as it has been reported for present debris-covered glaciers in the Himalaya (Benn and Owen, 2002). Here, medial flow lines can elevate debris towards the glacier margin (Boulton, 1978). Former glaciers in Limarí transported a mixture of angular to subrounded debris as observed on the LIM lateral moraine complexes. This boulder geometry denotes both a supraglacial passive and a subglacial active transport of debris sourced from the steep rock walls and at the subglacial bedrock, respectively. It is therefore stated that former glaciers in Limarí were mantled with debris that after deglaciation left a massive moraine deposit covering the valley bottoms and sides.

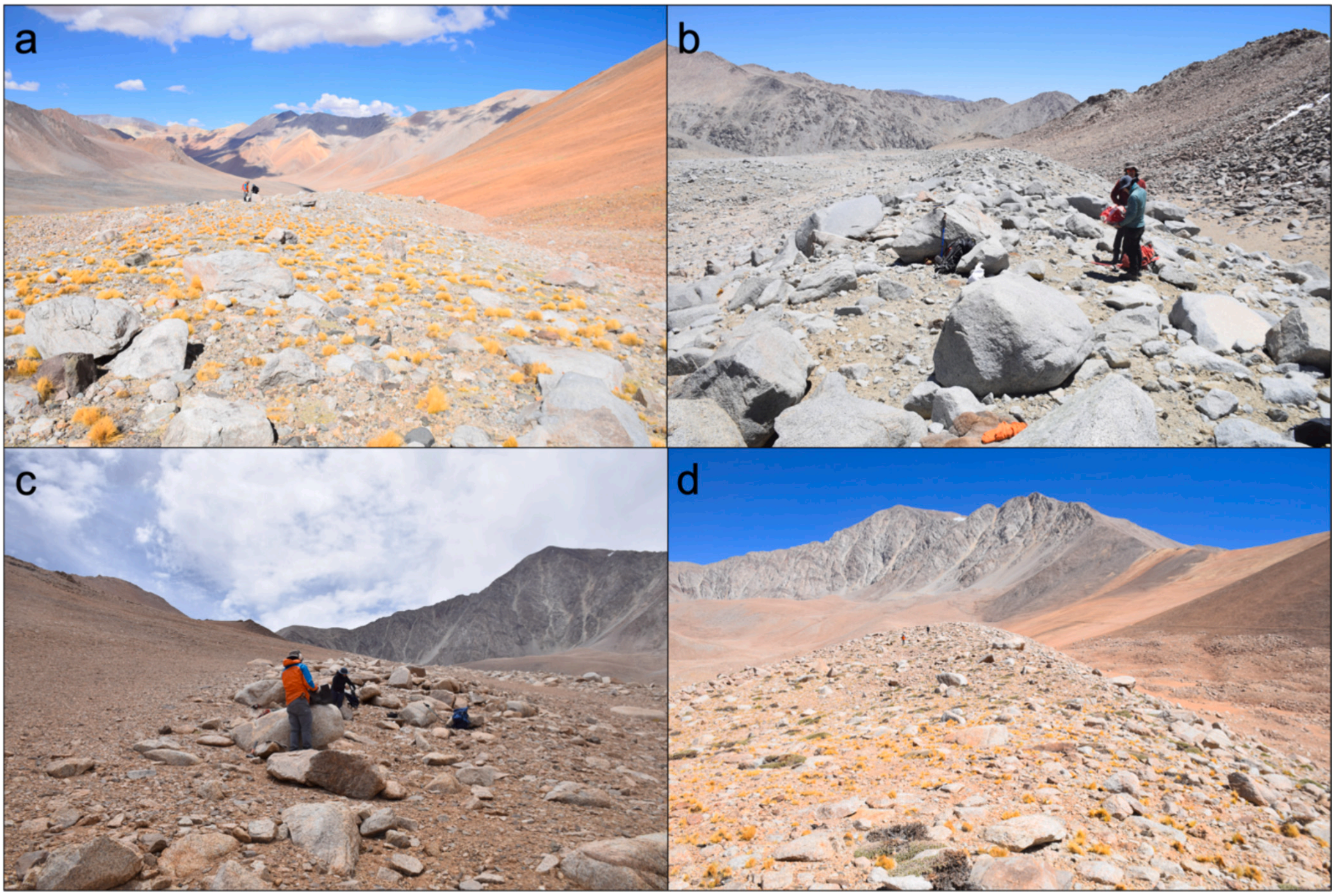

Fig. 9. The LIM II moraine landform in El Viento (a), El Toro (b) and El Despoblado (c and d).

Debris-covered glaciers are common in mountain regions with steep walls from where abundant debris can be delivered to the glacier surface (Mayr and Hagg, 2019). Glacier size, precipitation rates, and bedrock erodibility are other relevant factors (Benn and Owen, 2002). Debris mantle on glaciers occur in response to glacier melting and thinning in association with overall snout stagnation (Kirkbride and Deline, 2013). Increase of debris supply during deglacial stages may also be associated with a decrease of falling snow and warming of mountain permafrost (Deline, 2005). Former Limarí glaciers became debris-mantled in their snout and ablation zones during deglaciation in response to a negative mass balance, leaving the boulder-rich and extensive LIM II moraine landforms. Glaciers with debris cover are characterized by landforms that include lateral moraines, low-relief hummocky moraine, glacifluvial terraces, fluted moraines, and roches moutonnées (Benn and Owen, 2002), some of which are characteristic of the Limarí glacial geomorphic record (Carraha et al., 2024) and of other glacier forelands nearby (Zech et al., 2006, 2007; Fernández et al., 2022). The LIM II inboard concentric latero-frontal ridges record multiple long-term mass-balance cycles driving intercalated active transport and ablation-dominant conditions during overall deglaciation (Kirkbride and Deline, 2013; Fernández et al., 2022). The ridges themselves were formed by thickening and readvances of active ice with debris transport in response to a positive mass balance (Benn and Owen, 2002). Ablation areas of debris-mantled glaciers include active zones differentiated from inactive ice marginal zones without significant movement (Kirkbride and Deline, 2013). A slow-moving, thinning ice snout is potentially buried under debris with no significant change in its position (Naito et al., 2000). This can evolve to ice core marginal moraines that reflect an in-situ deglaciation dominated by downwasting of ice-cored landforms, disconnected from up-glacier active flow (Hambrey et al., 1997). The latter deposit can obstruct a following glacial expansion and add stress to longitudinal ice flow favoring elevation of basal debris to the glacier surface to develop a debris cover including subglacial subrounded boulders mixed with supraglacial angular ones as observed in Limarí (Figs. 8–12) (Kirkbride and Deline, 2013).

5.3. Glacial/periglacial interaction and transition

The widespread presence of permafrost-related-landforms on the valley slopes and, in particular, on LIM II moraines of the Limarí Basin, helps to better understand how glacial and periglacial domains transit from one to the other in response to climate change (Palacios et al., 2021). Moraines in Limarí show the geomorphic effect of permafrost, which implies that periglacial conditions followed deglaciation at the studied sites (Berthling, 2011; Murton, 2021). The geomorphic evidence for postglacial periglaciation and permafrost conditions in formerly glaciated areas of Limarí includes pervasive reworking of moraine debris by gelifluction and with viscous creep of perennially frozen materials (rock glaciers; Fig. 14) (Matsuoka, 2001; Lilleøren and Etzelmüller, 2011; Murton, 2021). Rework of till deposits by gelifluction is a common phenomenon where periglaciation postdate glaciation (Murton, 2021). Gelifluction lobes are indicative of periglacial terrain and linked to the active geomorphic effects of frozen ground on seasonal timescales (Matsuoka, 2001). Seasonally thawing of the active layer results in the downslope displacement of the plastic soil up to few decimeters in depth. This process may eventually yield medium-sized solifluction lobes as high as 30–200 cm (Matsuoka, 2001). The soil moisture content is critical for forming gelifluction lobes. Thus, seasonal thawing of the active layer implies the continuous availability of moisture during the frozen season, but also the addition of moisture from snowmelt as well (Matsuoka, 2001; Matthews and Nesje, 2022). The bouldery surface on a fine underlying sediment matrix making up the LIM II moraines, such as

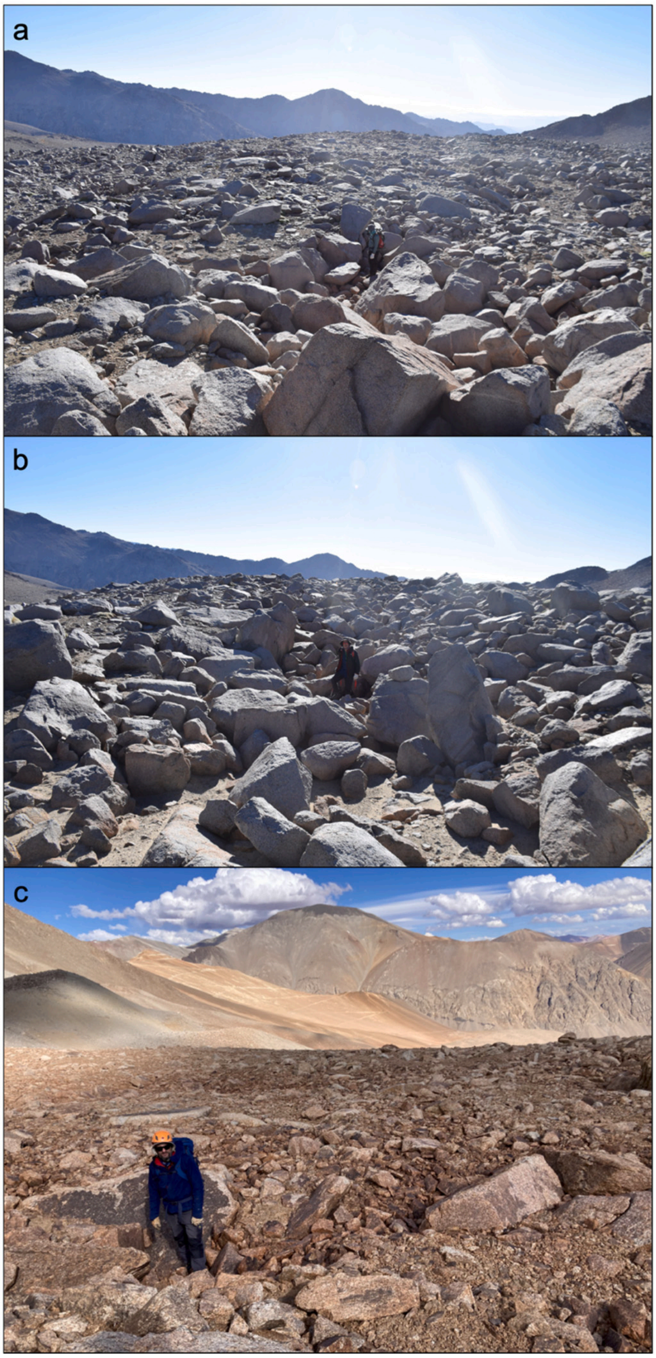

Fig. 10. Periglacial and in situ down-wasting features in LIM II moraine. **(a)** Meter-scale debris filled fractures on the TOR II moraine surface indicating periglacial ground deformation by frost-thaw action. Thermokarst subsidence type of features in the LIM II moraine at El Toro **(b)** and El Despoblado **(c)**.

TOR II, thus seems to have favored gelifluction and annual frost creep in a periglacial environment dominated by discontinuous permafrost (Fig. 14) (Murton, 2021).

Lower limits of rock glaciers with their typical surface patterns of ridges and furrows indicate lower limits of permafrost occurrence (Barsch, 1996). Viscous flow structures that characterize the TOR II moraine, are another expression of periglaciation of Limarí after deglaciation. These structures are more obvious in those areas where the moraine have steeper slopes (i.e., topographic steps) (Fig. 14). Slopes produce the critical driving stress for rock glacier-like features to form by cumulative deformation of ice-supersaturated perennially frozen materials (Barsch, 1996; Haeberli et al., 2006; Kenner and Magnusson, 2017). The implication is that the original glacial LIM II moraine was reworked into transversal viscous flow structures that expose the cohesive flow of rock glaciers (Haeberli et al., 2006). Although these structures appear somewhat degraded today, it is apparent that coherent creep under frozen conditions did reshape the moraine by transforming the original glacial deposit (Murton, 2021). The moraine surface is characterized by boulders of different sizes resting or embedded in a till matrix, but zones of former ground-ice creeping could also be evidenced in boulder-rich surface areas, where surficial fine sediment is less common (Amschwand et al., 2021). In addition, the superimposed coarse debris-filled fractures resembling frozen ground cracks suggest that periglaciation developed after moraine deposition (Murton, 2021). In similar manner, gelifluction deforming lateral moraines near the cirques indicate glaciers had totally abandoned the valleys when periglacial conditions affected the former glacier forefields (Fig. 14). Altogether, these periglacial-derived landforms reworking glacial moraines, indicate a glacial to interglacial transition in Limarí. Here, we mapped these features as moraine-related rock glacier (Figs. 3–6) and observe that boulder-rich hummocky moraines derived from debris-covered glaciers, which are abundant in many glaciated mountain areas (Mayr and Hagg, 2019), can be a niche for rock glaciers to form under prevailing permafrost conditions and slope-derived stress (Barsch, 1996). The geomorphic product is a composite landform including superimposed both glacially and periglacially derived aspects (Berthling, 2011; Lilleøren and Etzelmüller, 2011). It is not clear if paraglacial activity played any role in preconditioning the periglacial activity in the Limarí moraines because these glacial deposits remained disconnected from any potential rock failures from steep slopes (Matthews and Nesje, 2022). Our debris-covered glacier with rock glacier-type landforms can be interpreted as a sequence and transition of two independent events, and as that, it does not depend on the existence of a continuum of landforms (sensu Janke et al., 2015; Monnier and Kinnard, 2015). Rather, it requires the existence of regional-scale permafrost conditions affecting a moraine body forced by climate change for a certain time at the end of the last glaciation (Berthling, 2011). The key role relates to deep and slow freezing processes forced by the long-term existence of negative subsurface temperatures, i.e., permafrost (Berthling, 2011). Such long-term and deep freezing produces ice contents, which mostly by far exceed the pore volume of the original material in unfrozen conditions (cf. Hu et al., 2023). It is this excess ice or ice-supersaturation which fundamentally changes the geotechnical properties of the affected materials by inducing strong cohesion between individual rock particles, but also by reducing internal friction by separating of rock particles from each other (Springman et al., 2012). Such ice-rich frozen ground or “ice with rock inclusions” undergoes steady-state or secondary creep with unlimited, cumulative deformation. The formation of visually recognizable viscous landform features, however, requires combinations of stress-dependent creep rates and time (Haeberli et al., 2006).

5.4. Landform ages

5.4.1. LIM I moraine: pre-LGM glacier advance(s)

All ^{10}Be dates of the LIM I moraine at the three studied valleys (El Toro, Las Arenas, and El Viento) except for 1 sample (total of 18 ages) fall within the last glacial period chronozone (Marine Isotope Stage (MIS) 4 - MIS 2) (Jouzel et al., 2007). This implies that the LIM I moraine was deposited by glaciers that extended during pre-LGM times but within the last ice age in the headland of the Limarí Basin. The precise date of this advance cannot be constrained with the available scattered data. For instance, in TOR I the ^{10}Be age ranges between 41.2 ± 0.6 – 35.0 ± 0.5 ka, in LAR between 65.3 ± 1.0 – 24.9 ± 0.5 ka, and in EV between 94.2 ± 0.9 – 56.0 ± 0.6 ka. Several scenarios can be considered to explain the observed difference in ages among the LIM I moraines at the three valleys. First, LIM I does not represent one single generation of deposits but rather glacier advances at different times within the last ice

Fig. 11. Examples of sampled boulders in LIM I moraines and their surface exposure cosmogenic ages (in thousands of years ago; error 1 sigma).

Fig. 12. Examples of sampled boulders in LIM II moraines and their surface exposure cosmogenic ages (in thousands of years ago; error 1 sigma).

age (the elevation difference of these moraines supports this scenario). Second, LIM I could be a composite moraine ridge thus containing boulder surface exposure ages that represent more than one ice advance reaching the same ice margin several times within the last ice age. Third, in LIM I the distribution of ages results from unknown post-depositional geomorphic processes. Taking the TOR I data at face value, this moraine was deposited during the MIS 3, with most of the obtained exposure ages ranging between 41.2 ± 0.6 – 35.0 ± 0.5 ka (n = 3). Previously, Zech et al. (2007, 2017) obtained similar ^{10}Be ages for outer moraines marking the pre-LGM maximum glacial advance in the Cordón Doña Rosa. Their ^{10}Be ages point to a middle MIS 3 glacial advance, similar to our TOR I data, although Zech et al. (2007) indicate they should be referred as minimum ages for the associated glacial advance. Glacial advances punctuating the MIS 3 have been recorded in the southern Andes and elsewhere in the southern hemisphere and are not unexpected in the southern Andean Subtropics (Kelley et al., 2014; García et al., 2018, 2021).

5.4.2. *LIM II moraine: the LGM glacial advance*

Nearly 70 % of all samples obtained from moraine LIM II in all four studied valleys (El Toro, Las Arenas, El Viento, and El Despoblado) range between 24.2 ± 0.4 and 16.8 ± 0.2 ka (n = 38). The younger most frequent ^{10}Be ages of the outermost lateral moraines in Las Arenas, El Viento, and El Despoblado range between 18.7 and 18.5 ka. Those from the El Toro are discussed in the next section (5.4.3). The statistical mode for LIM II dates yielded 19.0 ka (Fig. 16), which indicates the most frequent date recorded in LIM II moraine. Hence, we conclude that LIM II moraine deposition occurred during a glacial expansion between 24.2

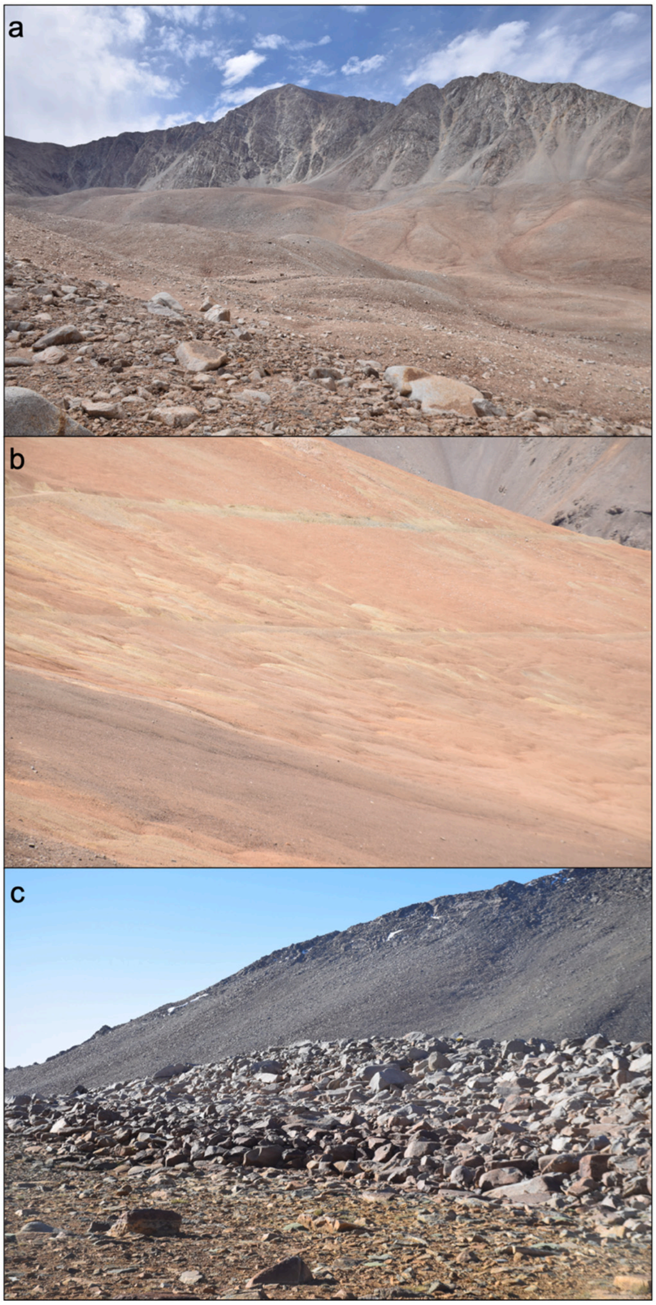

Fig. 13. Periglacial features in the Limari Basin. **(a)** Viscous flow derived landforms on the LIM II moraine in El Despoblado Valley; **(b)** Gelifluction lobes on the slope of the El Despoblado Valley. Lobes were cross-cut by the road; **(c)** Moraine-related rock glacier in Las Arenas.

± 0.4 and 18.6 ± 0.2 ka and culminated by 19 ka. ^{10}Be surface exposure data from glacially transported boulders near the cirque headwalls in El Toro indicate that complete glacier-free conditions were reached by 17.6 ± 0.2 ka in this valley, constraining the timing of the deglaciation in the cordillera. High-elevation and prominent moraine ridges enclosing cirques in other valleys, such as in El Despoblado, denote that small glaciers lingered longer after the LGM above ~4200 m a.s.l., but not below. Altogether, the implication is that we have dated the LIM II moraine to the global LGM chronozone (24–18 ka; Mix et al., 2001). In fact, the LIM II advance between 24.2 ± 0.4 and 18.6 ± 0.2 ka shows a striking correspondence to the global LGM period. Within this time range glaciers expanded in each of the valleys and then they melted out to leave a prominent moraine mantling the valley bottoms. Nearby glacial expansions within the LGM expose the regional scale of the LGM glacial advance in the subtropical Andes (Zech et al., 2017). Deglaciation was characterized by a steady ice retreat and thinning, and was completed by 17.6 ± 0.2 ka or earlier, leaving the main valleys glacier-free. Glacier ice abandonment of the Andean Encierro Valley (29° S) was recorded to occur in the same time range (18–17 ka) as based on ^{10}Be dating of boulders on moraines and scoured bedrock (Aguilar et al., 2022). All of our studied sites in Limarí are remarkably similar in their ^{10}Be chronological and geomorphic record, which supports our interpretation of the last glaciation and deglaciation fluctuation during the LGM and early Last Glacial Termination.

The samples yielding ages >28 ka in LIM II (n = 12) are rejected as outliers as they are significantly older than the main population of LIM II ages. These boulders have unknown geomorphic exposure histories. For instance, it is possible that the ^{10}Be inheritance of these boulders is associated to previous ice advances in the same valleys, and then reworked by the LGM glacial advance. Most of these outliers date to the MIS 3, corresponding to the age of LIM I advance in some of our sites in Limarí, and also similar to the outer moraines dated by Zech et al. (2007, 2017) in the region. On the other hand, we do not rule out that the ^{10}Be inheritance in these boulders could also be the response to other causes, including previous exposures on the headwalls or talus slopes before being delivered to the glacier surface or entrained by glacier erosion (Lehmann et al., 2022). In any case, these boulders were included by the LGM glacier expansion into the LIM II moraine, and they significantly overestimate the LGM age of this landform.

5.4.3. Late -Glacial periglaciation of the Limarí Andes

The younger ^{10}Be dates of exposure of the outer right lateral LIM II moraine in TOR Valley, ranging between 15.5 ± 0.3 and 13.6 ± 0.3 ka, can be potentially linked to the glacial to periglacial transition revealed by the geomorphic record. We hypothesize that these anomalous but consistent set of young ^{10}Be ages expose morphogenetic activity resulting as a consequence of periglacial geomorphic processes (Murton, 2021). These ^{10}Be samples were obtained from the top of a relatively steep section of the TOR II lateral ridge, a location susceptible of solifluction under seasonal frost and permafrost conditions (Matsuoka, 2001), potentially affecting the boulders stability and their exposure history. Thus, we posit these glacially deposited boulders were reworked by the effect of permafrost-related spatial displacements of frozen morainic material during the Late-Glacial time, thereby producing anomalously young exposure ages underestimating the LGM age of LIM II landform as dated elsewhere in all valleys. The Late-Glacial (~14.7–11.5 ka; Jouzel et al., 2007) is a global period of renewed low near glacial temperatures during the Last Glacial Termination (Denton et al., 2010) recorded by advanced glaciers in the Andes of central Chile (Fernández et al., 2021; Herrera-Ossandón et al., 2023), Patagonia, and elsewhere (Strelin et al., 2011; García et al., 2012; Sagredo et al., 2018). For instance, the Universidad Glacier at 34° S reached about 2/3 of its LGM extent during the Late-Glacial (Fernández et al., 2021). Opposite, the Limarí glaciers at 31° S had already abandoned the main valleys early after the LGM, as had also the Huasco glaciers to the north by c. 18 ka (Aguilar et al., 2022). Thus, a Late-glacial periglaciation seems to have dominated the high subtropical Andes in these formerly glaciated valleys.

5.5. Paleoclimate implications

The LGM in the Andean subtropics was a period with an estimated mean temperature depression of 5–6 °C and increased precipitation by ~100 % (Kull et al., 2002), comparable to other southern mid-latitude areas (Heusser et al., 1999; Putnam et al., 2013; Petherick et al., 2022). The Limarí LGM glaciers ended at ~3300 m a.s.l. close to the LGM permafrost limit ~3000–3300 m a.s.l. as estimated from the temperature depression reported by Kull et al. (2002). Under such thermal conditions with prevailing negative temperatures, LGM glaciers were

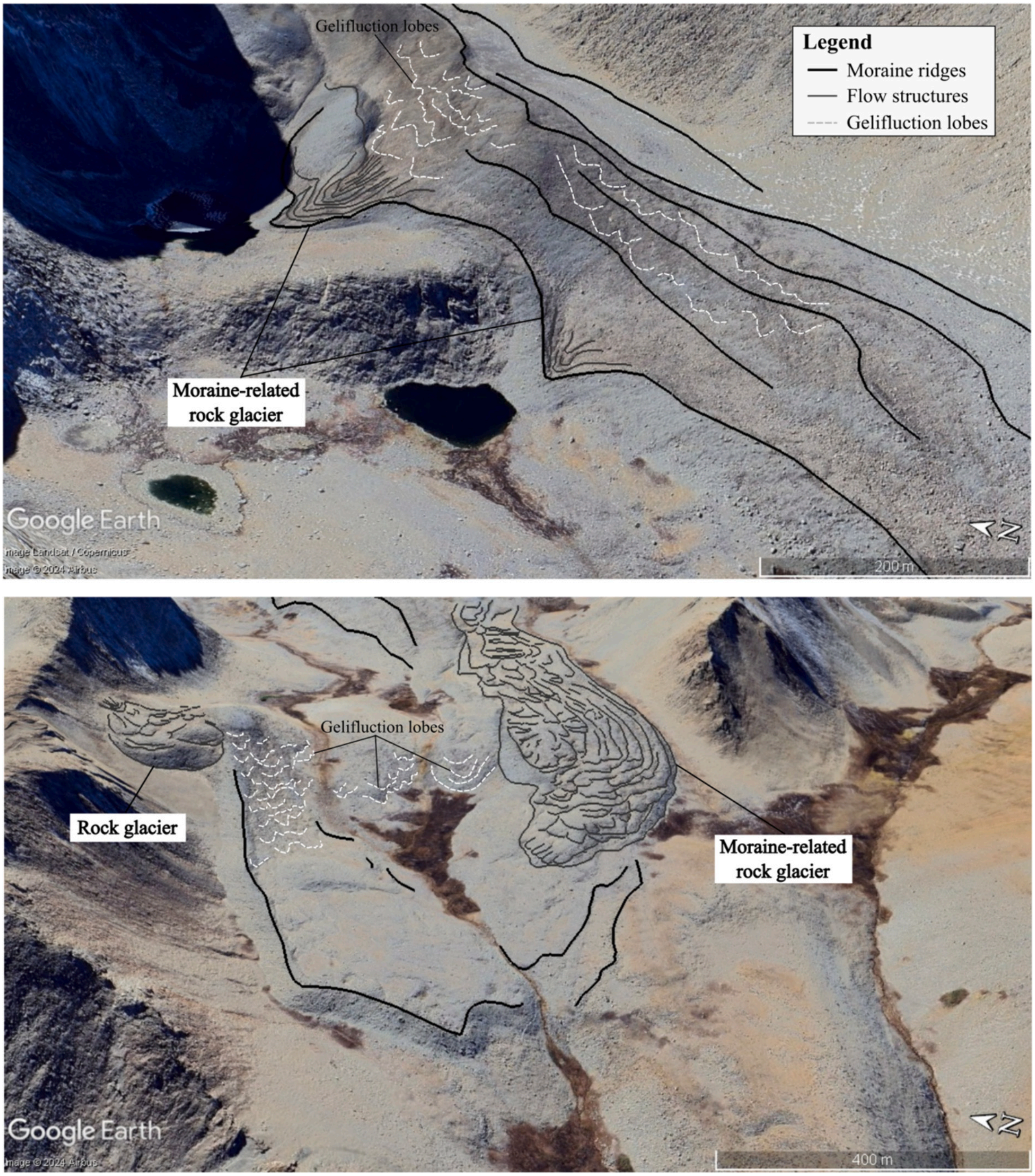

Fig. 14. Ice-rich viscous flow in the LIM II moraine in El Toro Valley. Permafrost type of flow structures and rock glaciers derived from left lateral moraines near the cirque (upper panel) and from the LIM II hummocky moraine at the valley bottom (lower panel). It is hypothesized that the observed ice-rich permafrost creeping occurred during the Late Glacial period in moraines deposited during the LGM.

likely polythermal with partially temperate firn areas but predominantly cold ablation areas (Cohen et al., 2018). The calculated ELA drop of ≥1000 m linked to lower temperatures and higher precipitation triggered an LGM glacier expansion in the semiarid subtropical Andes well-recorded in mountain chains worldwide and thus a global glacial event (Denton et al., 1999, 2021). The ELA, today at 5100–5300 m a.s.l., was lowered somewhat more than the lower permafrost limits, which is in accordance with more humid regional conditions during the LGM than today (Fig. 17). LGM-dated glacially polished boulders in the cirques of El Toro Valley (samples TOR2002, TOR2003, and TOR2004) point to warm-based glaciers at 3600–3700 m a.s.l., at or above the LGM ELA, which implies an ELA lowering of 1000–1500 m with respect to present. Again, the latter points to the effect of the global temperature drop and the regional increase in precipitation during the LGM. Similarly calculated ELAs have been estimated for Andean glaciers at 33° S (Herrera-Ossandón et al., 2023). Augmented precipitation in the Andes during the LGM was forced by a northern migration of the SWW in response to an expanded influence of the Antarctic realm through the ocean and atmosphere linking mid-to-high latitudes (Lamy et al., 2015). Several lines of evidence point to expanded SWW into lower latitudes prompting a colder and wetter LGM than present, including expanded glaciers, pollen, lacustrine sediment, and Bt paleosol development (Heusser et al., 1999; Kull et al., 2002; Valero-Garcés et al., 2005; García et al., 2019; Fernández et al., 2021; Aguilar et al., 2022). Moreover, marine

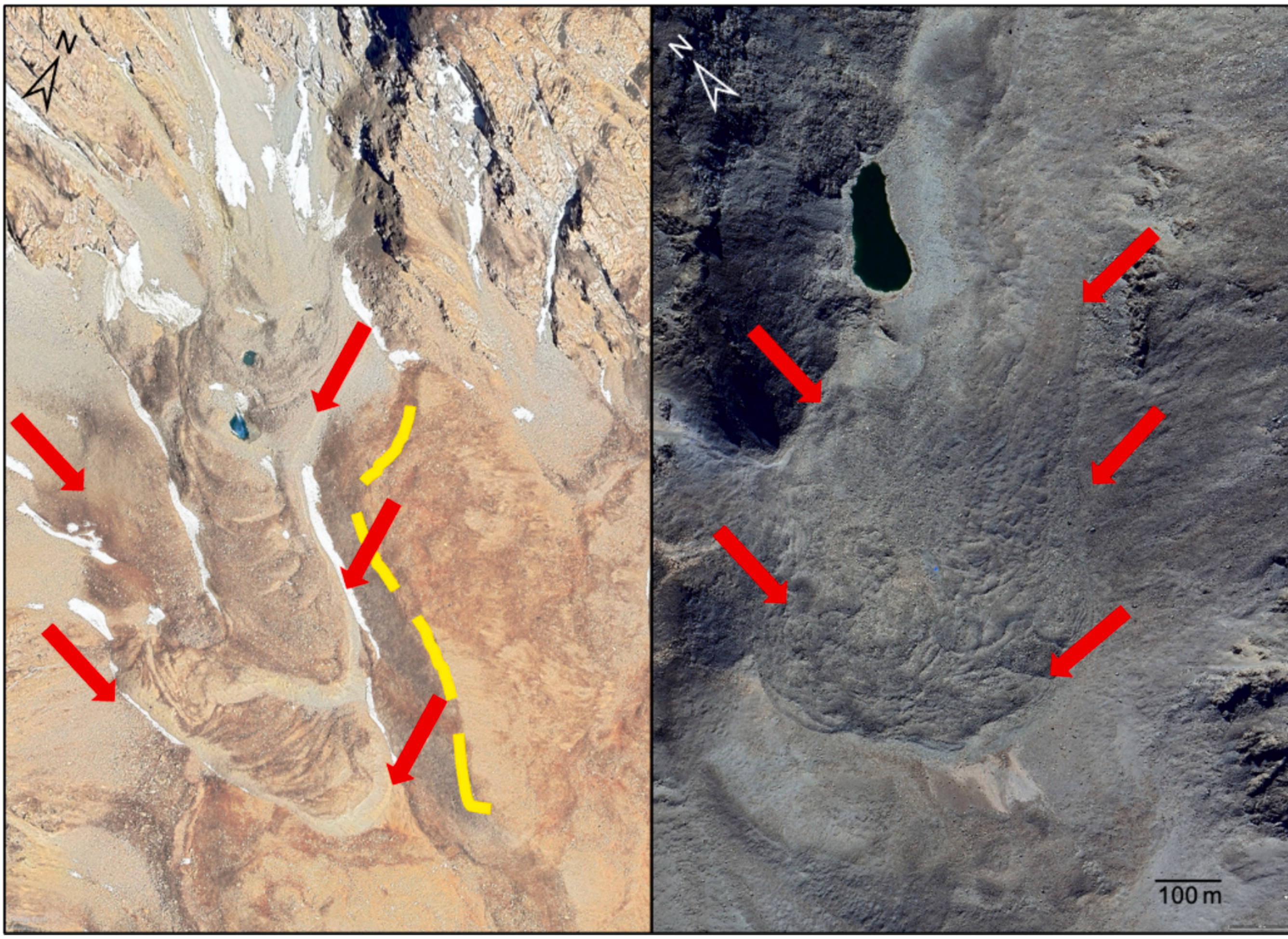

Fig. 15. Examples of rock glaciers in the Río Limarí Basin. Left: Active rock glacier extending down until 4320 m a.s.l. flanked by a lateral moraine ridge (right side of the rock glacier, segmented yellow line) in El Despoblado Valley (Río Hurtado). Right: Inactive rock glacier extending down until 3430 m a.s.l. north of the El Toro Valley (Combarbalá). Red arrows delimit the rock glaciers.

sediments also record a wetter climate during the LGM (e.g., Stuut and Lamy, 2004). After the LGM, global warming associated with a southern migration of the SWW and the expansion of the subtropical front triggered an ELA rise and glacier collapse early in the Last Glacial Termination (Denton et al., 2010; Palacios et al., 2023). Resumed cold and humid climate during the Late-Glacial affected again the southern middle latitudes but the effective moisture brought by the northward shifted SWW did not reach the Limarí Basin to produce significant glacier expansions here at 30–31° S, as it did further south (Fernández et al., 2021). Instead, we hypothesize the subtropical Andean glacial LGM deposits at ~3000–4000 m a.s.l. in Limarí were exposed to a cool and dry climate that prompted ice-rich permafrost creep processes and spatial displacements of frozen morainic material (Fig. 17). In other words, the reduction of precipitation after the LGM produced greater glacier retreat than permafrost retreat at higher altitudes. Our study exposes the central role of latitude and altitude thresholds in link with the position of the SWW in determining if glacial or periglacial conditions dominated the subtropical Andes at the end of the last ice age.

6. Conclusions

A total of 74 new ^{10}Be ages constrain the timing of glaciation, deglaciation, and glacial to periglacial transition denoted by the geomorphic imprint of the Limarí Basin in the subtropical semiarid Andes of northern Chile. Mountain glaciers expanded first during MIS 3 by 41.2 ± 0.6 – 35.0 ± 0.5 ka, and probably earlier as well. The next glacier advance occurred between 24.2 ± 0.4 and 18.6 ± 0.2 ka throughout the global LGM and culminated by 19 ka. Glacier retreat followed and by 17.6 ± 0.2 ka glaciers had already abandoned the valleys below ~4000 m a.s.l. early in the Last Glacial Termination. Our record of LGM and deglaciation nicely mimics the main global signal of glaciers, ice sheets, and sea-level change, evidencing interhemispheric near synchrony of climate forcing.

The LGM LIM II moraine was built as a composite landform that involved a sequence of glacial, deglacial, and periglacial morphogenetic processes. A massive hummocky moraine deposited by LGM debris-covered glaciers served afterwards during the Late-Glacial as a niche for seasonal frost and permafrost creep, which substantially modified the original landforms. The widespread development of solifluction and rock glaciers under permafrost conditions in glacially derived debris helps to understand the observed geomorphic record in the high Andes of Limarí and high mountains elsewhere that evidence glacial-periglacial transitions and interactions at the end of the ice age. There is a general lack of studies on debris-covered glaciers and their interaction with periglacial landforms in the subtropical Andes. Thus, this study contributes to a better understanding of the wide range of cryospheric landforms indicating the response to climate change in maritime dry mountain settings.

In particular, the studied glacial and periglacial geomorphic imprint denotes the sensitive response of the cryosphere of the subtropical Andes to the latitudinal migration of the southern westerly winds (SWW). The latitude and elevation factors determined if glacial or periglacial

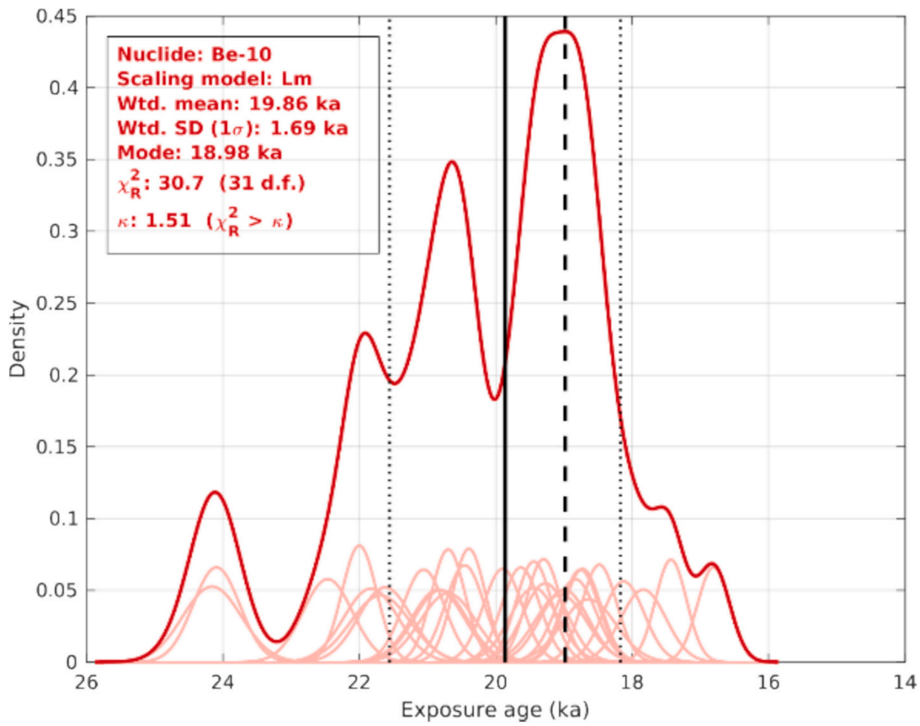

Fig. 16. ^{10}Be probability distribution of LIM II moraine including all four studied valleys, without outliers. The black dashed line is the mode, the black solid line is the weighted mean, and the black dotted lines are the weighted standard deviation. Plot obtained using iceTEA server (Jones et al., 2019; http://ice-tea.org).

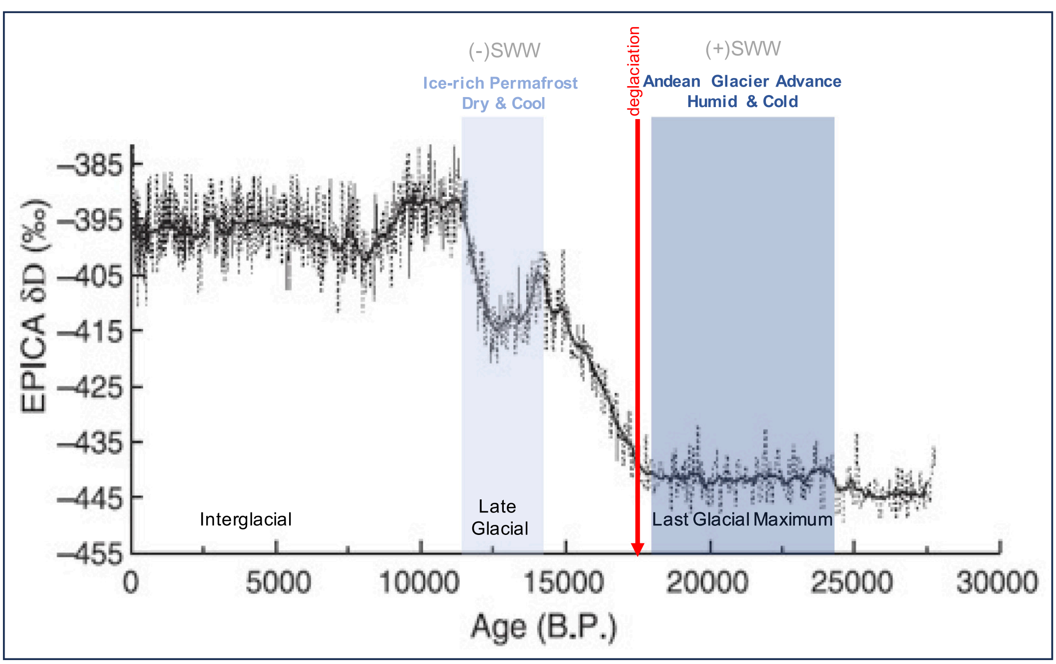

Fig. 17. Paleoclimate reconstruction in the subtropical Andes of Limarí Basin. Cold and humid climate triggered glacier advances during the LGM, but dry and cool conditions favored ice-rich permafrost during the Late Glacial when glacier ice had already mostly vanished. SWW: Southern Westerly Winds. (−) and (+) symbols categorize the influence of the SWW at different time periods at the study area. The Antarctic EPICA δD temperature record is from Stenni et al. (2001).

conditions controlled the geomorphic processes in the subtropical high Andes in link with the position of the SWW at the end of the last ice age. Further investigation is suggested for the periglacial landforms in the Andes in order to assess the geographic extent of the conclusions derived from this study.

Funding

This work was funded by the Fondo Nacional de Desarrollo Científico y Tecnológico (FONDECYT Regular Chile, grants #1200935 and #1241043) and the Swiss National Science Foundation (Grant IZSEZ0_215412).

CRediT authorship contribution statement

Juan-Luis García: Writing – original draft, Methodology, Investigation, Funding acquisition, Data curation, Conceptualization. **Javiera Carraha:** Writing – review & editing, Software, Investigation, Data curation. **Hans Fernández-Navarro:** Writing – review & editing, Methodology, Investigation. **Samuel U. Nussbaumer:** Writing – review & editing, Investigation. **Francia Pérez:** Writing – review & editing, Methodology. **Alan J. Hidy:** Writing – review & editing, Methodology. **Isabelle Gärtner-Roer:** Writing – review & editing, Validation. **Wilfried Haeberli:** Writing – review & editing, Validation, Investigation.

Declaration of competing interest

The authors declare that they have no known competing financial interests or personal relationships that could have appeared to influence the work reported in this paper.

Data availability

Data will be made available on request.

Acknowledgements

We acknowledge Diego Romero and Roberto Merino for their assistance during fieldwork. Further thanks go to Hacienda El Bosque for facilitating access to the study area and the local arrieros that provided assistance and campsites during field campaigns. We are very grateful to two anonymous reviewers whose comments helped to significantly improve the final version of the paper. This work was performed in part under the auspices of the U.S. Department of Energy by Lawrence Livermore National Laboratory under Contract DE-AC52-07NA27344; this is LLNL-JRNL-2000221.

References

Abele, G., 1984. Derrumbes de montaña y morrenas en los Andes chilenos. Rev. Geogr. Norte Gd. 11, 17–30.

Aguilar, G., Riquelme, R., Lohse, P., Cabré, A., García, J.L., 2022. Chronology of glacial advances and deglaciation in the Encierro River Valley (29° Lat. S), Southern Atacama Desert, based on geomorphological mapping and cosmogenic 10Be exposure ages. Front. Earth Sci. 10, 1–8. https://doi.org/10.3389/FEART.2022.878318.

Amschwand, D., Ivy-Ochs, S., Frehner, M., Steinemann, O., Christl, M., Vockenhuber, C., 2021. Deciphering the evolution of the Bleis Marscha rock glacier (Val d'Err, eastern Switzerland) with cosmogenic nuclide exposure dating, aerial image correlation, and finite element modeling. Cryosphere 15 (4), 2057–2081. https://doi.org/10.5194/TC-15-2057-2021.

Anderson, R.S., 2000. A model of ablation-dominated medial moraines and the generation of debris-mantled glacier snouts. J. Glaciol. 46 (154), 459–469. https://doi.org/10.3189/172756500781833025.

Antinao, J.L., Gosse, J., 2009. Large rockslides in the Southern Central Andes of Chile (32-34.5°S): tectonic control and significance for Quaternary landscape evolution. Geomorphology 104 (3–4), 117–133. https://doi.org/10.1016/j.geomorph.2008.08.008.

Azócar, G.F., Brenning, A., 2010. Hydrological and geomorphological significance of rock glaciers in the dry Andes, Chile (27°-33°S). Permafr. Periglac. Process. 21 (1), 42–53. https://doi.org/10.1002/ppp.669.

Balco, G., Stone, J.O., Lifton, N.A., Dunai, T.J., 2008. A complete and easily accessible means of calculating surface exposure ages or erosion rates from 10Be and 26Al measurements. Quat. Geochronol. 3 (3), 174–195. https://doi.org/10.1016/j.quageo.2007.12.001.

Ballantyne, C.K., 2002. Paraglacial geomorphology. Quat. Sci. Rev. 21 (18–19), 1935–2017. https://doi.org/10.1016/S0277-3791(02)00005-7.

Barsch, Dietrich, 1996. Rockglaciers : Indicators for the Present and Former Geoecology in High Mountain Environments, p. 331.

Benn, D.I., Owen, L.A., 2002. Himalayan glacial sedimentary environments: a framework for reconstructing and dating the former extent of glaciers in high mountains. Quat. Int. 97–98, 3–25. https://doi.org/10.1016/S1040-6182(02)00048-4.

Berthling, I., 2011. Beyond confusion: rock glaciers as cryo-conditioned landforms. Geomorphology 131 (3–4), 98–106. https://doi.org/10.1016/j.geomorph.2011.05.002.

Boulton, G.S., 1978. Boulder shapes and grain-size distributions of debris as indicators of transport paths through a glacier and till genesis. Sedimentology 25 (6), 773–799. https://doi.org/10.1111/J.1365-3091.1978.TB00329.X.

Brenning, A., 2005. Geomorphological, Hydrological and Climatic Significance of Rock Glaciers in the Andes of Central Chile (33-35∘S). Permafr. Periglac. Process. 16, 231–240. https://doi.org/10.1002/ppp.528.

Carraha, J., García, J.-L., Nussbaumer, S.U., Fernández-Navarro, H., Gärtner-Roer, I., 2024. Late Pleistocene to Holocene glacial, periglacial and paraglacial geomorphology of the upper Río Limarí basin (30-31°S) in the Andes of central Chile. J. Maps. https://doi.org/10.1080/17445647.2024.2329179.

Caviedes, C.N., Paskoff, R., 1975. Quaternary glaciations in the Andes of North-Central Chile. J. Glaciol. 14 (70), 153–174. https://doi.org/10.3189/S0022143000013472.

Charrier, R., Iturrizaga, L., Carretier, S., Regard, V., Charrier, R., Iturrizaga, L., Carretier, S., Regard, V., 2019. Evolución geomorfológica y glaciar de las hoyas de los ríos Maipo superior y Cachapoal en la Cordillera Principal Andina, Chile central (34°-35° S). Andean Geol. 46 (2), 240–278. https://doi.org/10.5027/ANDGEOV46N2-3108.

Clark, D.H., Steig, E.J., Potter, N., Fitzpatrick, J., Updike, A.B., Clark, G.M., 1996. Old ice in rock glaciers may provide long-term climate records. EOS Trans. Am. Geophys. Union 77 (23), 217–222. https://doi.org/10.1029/96EO00149.

Cohen, D., Gillet-Chaulet, F., Haeberli, W., Machguth, H., Fischer, U., 2018. Numerical reconstructions of the flow and basal conditions of the Rhine glacier, European Central Alps, at the Last Glacial Maximum. Cryosphere 12, 2515–2544. https://doi.org/10.5194/tc-12-2515-2018.

Colombo, N., Giaccone, E., Paro, L., Buffa, G., Fratianni, S., 2016. The recent transition from glacial to periglacial environment in a high altitude alpine basin (Sabbione basin, north-western Italian Alps). Preliminary outcomes from a multidisciplinary approach. Geogr. Fis. Din. Quat. 39 (1), 21–36. https://doi.org/10.4461/GFDQ.2016.39.3.

Deline, P., 2005. Change in surface debris cover on Mont Blanc massif glaciers after the "Little Ice Age" termination. Holocene 15 (2), 302–309. https://doi.org/10.1191/0959683605HL809RR.

Denton, G.H., Heusser, C.J., Lowel, T.V., Moreno, P.I., Andersen, B.G., Heusser, L.E., Schlüchter, C., Marchant, D.R., Sällskapet, S., 1999. Interhemispheric linkage of paleoclimate during the Last Glaciation. Geogr. Ann. A: Phys. Geogr. 81 (2), 107–153. https://doi.org/10.1111/1468-0459.00055.

Denton, G.H., Anderson, R.F., Toggweiler, J.R., Edwards, R.L., Schaefer, J.M., Putnam, A. E., 2010. The last glacial termination. Science 328 (5986), 1652–1656. https://doi.org/10.1126/science.1184119.

Denton, G.H., Putnam, A.E., Russell, J.L., Barrell, D.J.A., Schaefer, J.M., Kaplan, M.R., Strand, P.D., 2021. The Zealandia Switch: ice age climate shifts viewed from Southern Hemisphere moraines. Quat. Sci. Rev. 257, 106771 https://doi.org/10.1016/j.quascirev.2020.106771.

Dirección General de Aguas, 2022. Inventario Público de Glaciares. https://dga.mop.gob.cl.

Espizua, L.E., 1993. Quaternary glaciations in the Rio Mendoza Valley, Argentine Andes. Quat. Res. 40 (2), 150–162. https://doi.org/10.1006/QRES.1993.1067.

Etzelmüller, B., Frauenfelder, R., 2009. Factors controlling the distribution of mountain permafrost in the northern hemisphere and their influence on sediment transfer. Arct. Antarct. Alp. Res. 41 (1), 48–58. https://doi.org/10.1657/1523-0430-41.1.48.

Fernández, H., García, J.-L., Nussbaumer, S.U., Geiger, A., Gärtner-Roer, I., Tikhomirov, D., Egli, M., 2021. Last Glacial Maximum to near present 10Be chronology of the Universidad glacier fluctuations in the Subtropical Chilean Andes (34° S): paleoclimate implications. EGU21. https://doi.org/10.5194/EGUSPHERE-EGU21-13819.

Fernández, H., García, J.-L., Nussbaumer, S.U., Geiger, J., Gärtner-Roer, I., Pérez, F., Tikhomirov, D., Christl, M., Egli, M., 2022. De-icing landsystem model for the Universidad Glacier (34° S) in the Central Andes of Chile during the past ~660 years. Geomorphology 400, 1–17. https://doi.org/10.1016/j.geomorph.2021.108096.

Fernández-Navarro, H., García, J.L., Nussbaumer, S.U., Tikhomirov, D., Pérez, F., Gärtner-Roer, I., Christl, M., Egli, M., 2023. Fluctuations of the Universidad Glacier in the Andes of central Chile (34° S) during the latest Holocene derived from a 10Be moraine chronology. Quat. Sci. Rev. 300 https://doi.org/10.1016/J.QUASCIREV.2022.107884.

Frauenfelder, R., Kääb, A., 2000. Towards a palaeoclimatic model of rock-glacier formation in the Swiss Alps. Ann. Glaciol. 31, 281–286. https://doi.org/10.3189/172756400781820264.

García, A., Ulloa, C., Amigo, G., Milana, J.P., Medina, C., 2017. An inventory of cryospheric landforms in the arid diagonal of South America (high Central Andes, Atacama region, Chile). Quat. Int. 438, 4–19. https://doi.org/10.1016/J.QUAINT.2017.04.033.

García, J.L., Kaplan, M.R., Hall, B.L., Schaefer, J.M., Vega, R.M., Schwartz, R., Finkel, R., 2012. Glacier expansion in Southern Patagonia throughout the antarctic cold reversal. Geology 40 (9), 859–862. https://doi.org/10.1130/G33164.1.

García, J.L., Pizarro, F., Calcagni, V., 2014. Fluctuaciones glaciales holocénicas en el Cajón del Miapo, Andes Centrales de Chile: observaciones morfoestratigráficas de los glaciares Loma Larga y Nieves Negras. In: Borsdorf, A., Sánchez, R., Hidalgo, R., Zunino, H.M. (Eds.), Los riesgos traen oportunidades: Transformaciones globales en Los Andes sudamericanos, Serie GEOl, pp. 35–52. https://www.researchgate.net/publication/267268320.

García, J.L., Hein, A.S., Binnie, S.A., Gómez, G.A., González, M.A., Dunai, T.J., 2018. The MIS 3 maximum of the Torres del Paine and Última Esperanza ice lobes in Patagonia and the pacing of southern mountain glaciation. Quat. Sci. Rev. 185, 9–26. https://doi.org/10.1016/J.QUASCIREV.2018.01.013.

García, J.L., Andrade, B., Calderón, M., Lüthgens, C., 2019. Multi-millennial scale climate variability during MIS 3 and MIS 2 inferred from luminescence dating of coastal sand dunes and buried paleosol sequences in central Chile, 32°S. J. Quat. Sci. 34, 203–214. https://doi.org/10.1002/jqs.3092.

García, J.L., Lüthgens, C., Vega, R.M., Rodés, Á., Hein, A.S., Binnie, S.A., 2021.

A composite 10Be, IR-50 and 14C chronology of the pre-Last Glacial Maximum (LGM) full ice extent of the western Patagonian Ice Sheet on the Isla de Chiloé, south Chile (42°S). E G Quat. Sci. J. 70 (1), 105–128. https://doi.org/10.5194/egqsj-70-105-2021.

Garreaud, R.D., 2009. The Andes climate and weather. Adv. Geosci. 22, 3–11. https://doi.org/10.5194/adgeo-22-3-2009.

Gärtner-Roer, I., Brunner, N., Delaloye, R., Haeberli, W., Kaab, A., Thee, P., 2022. Glacier-permafrost relations in a high-mountain environment: 5 decades of kinematic monitoring at the Gruben site, Swiss Alps. Cryosphere 16 (5), 2083–2101. https://doi.org/10.5194/TC-16-2083-2022.

Gómez, G.A., García, J.L., Villagrán, C., Lüthgens, C., Abarzúa, A.M., 2022. Vegetation, glacier, and climate changes before the global last glacial maximum in the Isla Grande de Chiloé, southern Chile (42° S). Quat. Sci. Rev. 276, 107301 https://doi.org/10.1016/J.QUASCIREV.2021.107301.

Haeberli, W., Beniston, M., 1998. Climate change and its impacts on glaciers and permafrost in the Alps. Ambio 27 (4), 258–265. https://www.jstor.org/stable/4314732.

Haeberli, W., Burn, C.R., 2002. Natural hazards in forests: glacier and permafrost effects as related to climate change. In: Environmental Changes and Geomorphic Hazards in Forests, 167–202. https://doi.org/10.1079/9780851995984.0167.

Haeberli, W., Vonder Mühll, D., 1996. On the characteristics and possible origin of ice in rock glacier permafrost. Z. Geomorphol. NF 104, 43–56.

Haeberli, W., Hallet, B., Arenson, L., Elconin, R., Humlum, O., Kääb, A., Kaufmann, V., Ladanyi, B., Matsuoka, N., Springman, S., Vonder Mühll, D., 2006. Permafrost creep and rock glacier dynamics. Permafr. Periglac. Process. 17 (3), 189–214. https://doi.org/10.1002/ppp.561.

Haeberli, W., Arenson, L.U., Wee, J., Hauck, C., Mölg, N., 2024. Discriminating viscous-creep features (rock glaciers) in mountain permafrost from debris-covered glaciers - a commented test at the Gruben and Yerba Loca sites, Swiss Alps and Chilean Andes. Cryosphere 18 (4), 1669–1683. https://doi.org/10.5194/TC-18-1669-2024.

Hambrey, M.J., Huddart, D., Bennett, M.R., Glasser, N.F., 1997. Genesis of "hummocky moraines" by thrusting in glacier ice: evidence from Svalbard and Britain. J. Geol. Soc. Lond. 154 (4), 623–632. https://doi.org/10.1144/gsjgs.154.4.0623.

Hambrey, M.J., Bennett, M.R., Dowdeswell, J.A., Glasser, N.F., Huddart, D., 1999. Debris entrainment and transfer in polythermal valley glaciers. J. Glaciol. 45 (149), 69–86. https://doi.org/10.1017/s0022143000003051.

Harrison, S., Whalley, B., Anderson, E., 2008. Relict rock glaciers and protalus lobes in the British Isles: implications for Late Pleistocene mountain geomorphology and palaeoclimate. J. Quat. Sci. 23 (3), 287–304. https://doi.org/10.1002/jqs.1148.

Hendrickx, H., Jacob, M., Frankl, A., Nyssen, J., Hendrickx, H., Jacob, M., Frankl, A., Nyssen, J., 2015. Glacial and periglacial geomorphology and its paleoclimatological significance in three North Ethiopian Mountains, including a detailed geomorphological map. Geomorphology 246, 156–167. https://doi.org/10.1016/J.GEOMORPH.2015.05.005.

Herrera-Ossandón, M., Easton, G., Antinao, J.L., Forman, S.L., 2023. Late Quaternary glacier advances in the Andes of Santiago, central Chile, and paleoclimatic implications. Front. Earth Sci. 11, 1192812 https://doi.org/10.3389/feart.2023.1192812.

Heusser, C.J., Heusser, L.E., Lowell, L.E., 1999. Paleoecology of the southern chilean lake district-isla grande de Chiloé during middle–late Llanquihue glaciation and deglaciation. Geogr. Ann. Ser. A Phys. Geogr. 81A, 231-284. https://www.tandfonline.com/doi/abs/10.1111/1468-0459.00058.

Hock, R., Rasul, G., Adler, C., Cáceres, B., Gruber, S., Hirabayashi, Y., Jackson, M., Kääb, A., Kang, S., Kutuzov, S., Milner, A., Molau, U., Morin, S., Orlove, B., Steltzer, H., 2022. High mountain areas. In: The Ocean and Cryosphere in a Changing Climate. Cambridge University Press, pp. 131–202. https://doi.org/10.1017/9781009157964.004.

Hu, Y., Harrison, S., Liu, L., Wood, J.L., 2023. Modelling rock glacier ice content based on InSAR-derived velocity, Khumbu and Lhotse valleys, Nepal. Cryosphere 17 (6), 2305–2321. https://doi.org/10.5194/tc-17-2305-2023.

Instituto Argentino de Nivología, 2018. Glaciología y Ciencias Ambientales. Inventario Nacional de Glaciares.

Janke, J.R., Bellisario, A.C., Ferrando, F.A., 2015. Classification of debris-covered glaciers and rock glaciers in the Andes of central Chile. In: Geomorphology, vol. 241. Elsevier, pp. 98–121. https://doi.org/10.1016/j.geomorph.2015.03.034.

Jones, R.S., Small, D., Cahill, N., Bentley, M.J., Whitehouse, P.L., 2019. iceTEA: tools for plotting and analysing cosmogenic-nuclide surface-exposure data from former ice margins. Quat. Geochronol. 51, 72–86. https://doi.org/10.1016/j.quageo.2019.01.001.

Jouzel, J., Masson-Delmotte, V., Cattani, O., Dreyfus, G., Falourd, S., Hoffmann, G., Minster, B., Nouet, J., Barnola, J.M., Chappellaz, J., Fischer, H., Gallet, J.C., Johnsen, S., Leuenberger, M., Loulergue, L., Luethi, D., Oerter, H., Parrenin, F., Raisbeck, G., Wolff, E.W., 2007. Orbital and millennial Antarctic climate variability over the past 800,000 years. Science 317 (5839), 793–796. https://doi.org/10.1126/SCIENCE.1141038.

Kaplan, M.R., Strelin, J.A., Schaefer, J.M., Denton, G.H., Finkel, R.C., Schwartz, R., Putnam, A.E., Vandergoes, M.J., Goehring, B.M., Travis, S.G., 2011. In-situ cosmogenic 10Be production rate at Lago Argentino, Patagonia: implications for late-glacial climate chronology. Earth Planet. Sci. Lett. 309 (1–2), 21–32. https://doi.org/10.1016/j.epsl.2011.06.018.

Kelley, S.E., Kaplan, M.R., Schafer, J.M., Andersen, B.G., Barrell, D.J.A., Putnam, A.E., Denton, G.H., Schwartz, R., Finkel, R.C., Doughty, A.M., 2014. High-precision 10Be chronology of moraines in the Southern Alps indicates synchronous cooling in Antarctica and New Zealand 42,000 years ago. Earth Planet. Sci. Lett. 405, 194–206. https://doi.org/10.1016/j.epsl.2014.07.031.

Kenner, R., Magnusson, J., 2017. Estimating the effect of different influencing factors on rock glacier development in two regions in the Swiss Alps. Permafr. Periglac. Process. 28 (1), 195–208. https://doi.org/10.1002/PPP.1910.

Kirkbride, M.P., Deline, P., 2013. The formation of supraglacial debris covers by primary dispersal from transverse englacial debris bands. Earth Surf. Process. Landf. 38 (15), 1779–1792. https://doi.org/10.1002/esp.3416.

Kjær, K.H., Krüger, J., 2001. The final phase of dead-ice moraine development: processes and sediment architecture, Kötlujökull, Iceland. Sedimentology 48 (5), 935–952. https://doi.org/10.1046/J.1365-3091.2001.00402.X.

Kohl, C.P., Nishiizumi, K., 1992. Chemical isolation of quartz for measurement of in-situ-produced cosmogenic nuclides. Geochim. Cosmochim. Acta (United States) 56:9 (9), 3583–3587. https://doi.org/10.1016/0016-7037(92)90401-4.

Kull, C., Grosjean, M., Veit, H., 2002. Modeling modern and Late Pleistocene Glacio-Climatological conditions in the North Chilean Andes (29-30° S). Clim. Chang. 52 (3), 359–381. https://doi.org/10.1023/A:1013746917257.

Lal, D., 1991. Cosmic ray labeling of erosion surfaces: in situ nuclide production rates and erosion models. Earth Planet. Sci. Lett. 104 (2–4), 424–439. https://doi.org/10.1016/0012-821X(91)90220-C.

Lamy, F., Arz, H.W., Kilian, R., Lange, C.B., Lembke-Jene, L., Wengler, M., Kaiser, J., Baeza-Urrea, O., Hall, I.R., Harada, N., Tiedemann, R., 2015. Glacial reduction and millennial-scale variations in Drake Passage throughflow. Proc. Natl. Acad. Sci. USA 112 (44), 13496–13501. https://doi.org/10.1073/PNAS.1509203112.

Lehmann, B., Anderson, R.S., Bodin, X., Cusicanqui, D., Valla, P.G., Carcaillet, J., 2022. Alpine rock glacier activity over Holocene to modern timescales (western French Alps). Earth Surf. Dyn. 10 (3), 605–633. https://doi.org/10.5194/ESURF-10-605-2022.

Lifton, N., Sato, T., Dunai, T.J., 2014. Scaling in situ cosmogenic nuclide production rates using analytical approximations to atmospheric cosmic-ray fluxes. Earth Planet. Sci. Lett. 386, 149–160. https://doi.org/10.1016/j.epsl.2013.10.052.

Lilleøren, K.S., Etzelmüller, B., 2011. A regional inventory of rock glaciers and ice-cored moraines in Norway. Geogr. Ann. A: Phys. Geogr. 93 (3), 175–191. https://doi.org/10.1111/j.1468-0459.2011.00430.x.

Lira, M.P., García, J.L., Bentley, M.J., Jamieson, S.S.R., Darvill, C.M., Hein, A.S., Fernández, H., Rodés, Á., Fabel, D., Smedley, R.K., Binnie, S.A., 2022. The Last Glacial Maximum and deglacial history of the Seno Skyring Ice Lobe (52°S), Southern Patagonia. Front. Earth Sci. 10, 892316 https://doi.org/10.3389/feart.2022.892316.

Masiokas, M.H., Rabatel, A., Rivera, A., Ruiz, L., Pitte, P., Ceballos, J.L., Barcaza, G., Soruco, A., Bown, F., Berthier, E., Dussaillant, I., MacDonell, S., 2020. A review of the current state and recent changes of the Andean cryosphere. In: Frontiers in Earth Science, vol. 8. Frontiers Media S.A. https://doi.org/10.3389/feart.2020.00099

Matsuoka, N., 2001. Solifluction rates, processes and landforms: a global review. Earth Sci. Rev. 55 (1–2), 107–134. https://doi.org/10.1016/S0012-8252(01)00057-5.

Matthews, J.A., Nesje, A., 2022. Scandinavia. In: Oliva, M., Nývlt, D., Fernández-Fernández, J.M. (Eds.), Periglacial Landscapes of Europe. Springer.

Matthews, J.A., Wilson, P., Mourne, R.W., 2017. Landform transitions from pronival ramparts to moraines and rock glaciers: a case study from the Smørbotn cirque, Romsdalsalpane, southern Norway. Geogr. Ann. A: Phys. Geogr. 99 (1), 15–37. https://doi.org/10.1080/04353676.2016.1256582.

Mayr, E., Hagg, W., 2019. Debris-covered glaciers. In: Heckmann, T., Morche, D. (Eds.), Geomorphology of Proglacial Systems, pp. 59–71. https://doi.org/10.1007/978-3-319-94184-4_4.

Mix, A.C., Bard, E., Schneider, R., 2001. Environmental processes of the ice age: land, oceans, glaciers (EPILOG). Quat. Sci. Rev. 20, 627–657. https://doi.org/10.1016/S0277-3791(00)00145-1.

Monnier, S., Kinnard, C., 2015. Reconsidering the glacier to rock glacier transformation problem: new insights from the central Andes of Chile. Geomorphology 238, 47–55. https://doi.org/10.1016/j.geomorph.2015.02.025.

Monnier, S., Kinnard, C., Surazakov, A., Bossy, W., 2014. Geomorphology, internal structure, and successive development of a glacier foreland in the semiarid Chilean Andes (Cerro Tapado, upper Elqui Valley, 30°08′ S., 69°55′ W.). Geomorphology 207, 126–140. https://doi.org/10.1016/j.geomorph.2013.10.031.

Moreiras, S.M., Hermanns, R.L., Fauqué, L., 2015. Cosmogenic dating of rock avalanches constraining Quaternary stratigraphy and regional neotectonics in the Argentine Central Andes (32° S). Quat. Sci. Rev. 112, 45–58. https://doi.org/10.1016/j.quascirev.2015.01.016.

Murton, J.B., 2021. What and where are periglacial landscapes? Permafr. Periglac. Process. 32 (2), 186–212. https://doi.org/10.1002/ppp.2102.

Naito, N., Nakawo, M., Kadota, T., Raymond, C.F., 2000. Numerical simulation of recent shrinkage of Khumbu Glacier, Nepal Himalayas. In: Nakawo, M., Raymond, C.F., Fountain, A. (Eds.), Debris-covered Glaciers, vol. Issue 264. IAHS Press, pp. 245–254.

Nishiizumi, K., Imamura, M., Caffee, M.W., Southon, J.R., Finkel, R.C., McAninch, J., 2007. Absolute calibration of 10Be AMS standards. Nucl. Instrum. Methods Phys. Res., Sect. B 258 (2), 403–413. https://doi.org/10.1016/J.NIMB.2007.01.297.

Oliva, M., Fernandes, M., Palacios, D., Fernández-Fernández, J.M., Schimmelpfennig, I., Antoniades, D., Aumaître, G., Bourlès, D., Keddadouche, K., 2021. Rapid deglaciation during the Bølling-Allerød Interstadial in the Central Pyrenees and associated glacial and periglacial landforms. Geomorphology 385, 107735. https://doi.org/10.1016/J.GEOMORPH.2021.107735.

Palacios, D., Rodríguez-Mena, M., Fernández-Fernández, J.M., Schimmelpfennig, I., Tanarro, L.M., Zamorano, J.J., Andrés, N., Úbeda, J., Saemundsson, Þ., Brynjólfsson, S., Oliva, M., Team, A., 2021. Reversible glacial-periglacial transition in response to climate changes and paraglacial dynamics: a case study from Héðinsdalsjökull (northern Iceland). Geomorphology 388, 1–22. https://doi.org/10.1016/j.geomorph.2021.107787.

Palacios, D., Hughes, P.D., Sánchez-Goñi, M.F., García-Ruiz, J.M., Andrés, N., 2022. The terminations of the glacial cycles. In: European Glacial Landscapes: The Last Deglaciation, 11–24. https://doi.org/10.1016/B978-0-323-91899-2.00002-4.

Palacios, D., Hughes, P.D., Sánchez-Goñi, M.F., García-Ruiz, J.M., Andrés, N., 2023. The terminations of the glacial cycles. In: European Glacial Landscapes: The Last Deglaciation. Elsevier, pp. 11–24. https://doi.org/10.1016/B978-0-323-91899-2.00002-4.

Paskoff, R.P., 1977. Quaternary of Chile: the state of research. Quat. Res. 8 (1), 2–31. https://doi.org/10.1016/0033-5894(77)90054-0.

Petherick, L.M., Knight, J., Shulmeister, J., Bostock, H., Lorrey, A., Fitchett, J., Turney, C., 2022. An extended last glacial maximum in the Southern Hemisphere: A contribution to the SHeMax project. Earth Sci. Rev. 231, 104090 https://doi.org/10.1016/j.earscirev.2022.104090.

Putnam, A.E., Schaefer, J.M., Denton, G.H., Barrell, D.J.A., Birkel, S.D., Andersen, B.G., Kaplan, M.R., Finkel, R.C., Schwartz, R., Doughty, A.M., 2013. The Last Glacial Maximum at 44°S documented by a 10Be moraine chronology at Lake Ohau, Southern Alps of New Zealand. Quat. Sci. Rev. 62, 114–141. https://doi.org/10.1016/j.quascirev.2012.10.034.

Quintana, J.M., Aceituno, P., 2012. Changes in the rainfall regime along the extratropical west coast of South America (Chile): 30-43° S. S Atmósfera 25 (1), 1–22. https://www.scielo.org.mx/pdf/atm/v25n1/v25n1a1.pdf.

Sagredo, E.A., Lowell, T.V., 2012. Climatology of Andean glaciers: a framework to understand glacier response to climate change. Glob. Planet. Chang. 86–87, 101–109. https://doi.org/10.1016/j.gloplacha.2012.02.010.

Sagredo, E.A., Kaplan, M.R., Araya, P.S., Lowell, T.V., Aravena, J.C., Moreno, P.I., Kelly, M.A., Schaefer, J.M., 2018. Trans-pacific glacial response to the Antarctic Cold Reversal in the southern mid-latitudes. Quat. Sci. Rev. 188, 160–166. https://doi.org/10.1016/j.quascirev.2018.01.011.

Santana, R., 1967. Rasgos de la glaciación cuaternaria en El Manzanar, Valle del Cachapoal, Andes de Rancagua. Rev. geogr. Valpso. 1, 85–98.

Sattler, K., Anderson, B., Mackintosh, A., Norton, K., de Róiste, M., 2016. Estimating permafrost distribution in the maritime southern alps, New Zealand, based on climatic conditions at rock glacier sites. Front. Earth Sci. 4, 166178 https://doi.org/10.3389/feart.2016.00004.

Seppi, R., Zanoner, T., Carton, A., Bondesan, A., Francese, R., Carturan, L., Zumiani, M., Giorgi, M., Ninfo, A., 2014. Current transition from glacial to periglacial processes in the Dolomites (South-Eastern Alps). Geomorphology 228, 71–86. https://doi.org/10.1016/j.geomorph.2014.08.025.

SERNAGEOMIN, 2006. Mapa Geológico de Chile (In REPUBLICA DE CHILE).

Shroder, J.F., Bishop, M.P., Copland, L., Sloan, V.F., 2000. Debris-covered glaciers and rock glaciers in the Nanga Parbat Himalaya, Pakistan. Pakistan. Geogr. Ann. 82 (1), 17–31. https://doi.org/10.1111/j.0435-3676.2000.00108.x.

Springman, S.M., Arenson, L.U., Yamamoto, Y., Maurer, H., Kos, A., Buchli, T., Derungs, G., 2012. Multidisciplinary investigations on three rock glaciers in the swiss alps: legacies and future perspectives. Geogr. Ann. A: Phys. Geogr. 94 (2), 215–243. https://doi.org/10.1111/j.1468-0459.2012.00464.x.

Stenni, B., Masson-Delmotte, V., Johnsen, S., Jouzel, J., Longinelli, A., Monnin, E., Selmo, E., 2001. An oceanic cold reversal during the last deglaciation. Science 293 (5537), 2074–2077. https://doi.org/10.1126/science.1059702.

Stone, J.O., 2000. Air pressure and cosmogenic isotope production. J. Geophys. Res. Solid Earth 105 (B10), 23753–23759. https://doi.org/10.1029/2000JB900181.

Strelin, J.A., Denton, G.H., Vandergoes, M.J., Ninnemann, U.S., Putnam, A.E., 2011. Radiocarbon chronology of the late-glacial Puerto Bandera moraines, Southern Patagonian Icefield, Argentina. Quat. Sci. Rev. 30 (19–20), 2551–2569. https://doi.org/10.1016/j.quascirev.2011.05.004.

Stuut, J.B.W., Lamy, F., 2004. Climate variability at the southern boundaries of the Namib (southwestern Africa) and Atacama (northern Chile) coastal deserts during the last 120,000 yr. Quat. Res. 62 (3), 301–309. https://doi.org/10.1016/J.YQRES.2004.08.001.

Trombotto, D., 2000. Survey of cryogenic processes, periglacial forms and permafrost conditions in South America. Rev. Inst. Geol. 21 (1–2), 33–55. https://doi.org/10.5935/0100-929X.20000004.

Trombotto, D., Buk, E., Hernández, J., 1997. Monitoring of mountain permafrost in the Central Andes, Cordon del Plata, Mendoza, Argentina. Permafr. Periglac. Process. 8, 123–129. https://doi.org/10.1002/(SICI)1099-1530(199701)8:13.0.CO;2-M.

Valero-Garcés, B.L., Jenny, B., Rondanelli, M., Delgado-Huertas, A., Burns, S.J., Veit, H., Moreno, A., 2005. Palaeohydrology of Laguna de Tagua Tagua (34° 30′ S) and moisture fluctuations in Central Chile for the last 46 000 yr. J. Quat. Sci. 20 (7–8), 625–641. https://doi.org/10.1002/jqs.988.

Veit, H., Preusser, F., Trauerstein, M., 2015. The Southern Westerlies in Central Chile during the two last glacial cycles as documented by coastal aeolian sand deposits and intercalating palaeosols. CATENA 134, 30–40. https://doi.org/10.1016/J.CATENA.2014.11.002.

Vicuña, S., Garreaud, R.D., McPhee, J., 2011. Climate change impacts on the hydrology of a snowmelt driven basin in semiarid Chile. Clim. Chang. 105 (3–4), 469–488. https://doi.org/10.1007/s10584-010-9888-4.

Vivero, S., Bodin, X., Farías-Barahona, D., MacDonell, S., Schaffer, N., Robson, B.A., Lambiel, C., 2021. Combination of aerial, satellite, and UAV photogrammetry for quantifying rock glacier kinematics in the Dry Andes of Chile (30°S) since the 1950s. Front. Remote Sens. 2, 784015 https://doi.org/10.3389/FRSEN.2021.784015.

Zech, J., Terrizzano, C., García-Morabito, E., Veit, H., Zech, R., 2017. Timing and extent of late pleistocene glaciation in the arid central Andes of Argentina and Chile (22°-41°S). Cuad. Investig. Geogr. 43 (2), 697–718. https://doi.org/10.18172/cig.3235.

Zech, R., Kull, C., Veit, H., 2006. Late Quaternary glacial history in the Encierro Valley, northern Chile (29°S), deduced from 10 Be surface exposure dating. Palaeogeogr. Palaeoclimatol. Palaeoecol. 234, 277–286. https://doi.org/10.1016/j.palaeo.2005.10.011.

Zech, R., Kull, C., Kubik, P.W., Veit, H., 2007. Exposure dating of Late Glacial and pre-LGM moraines in the Cordon de Doña Rosa, Northern/Central Chile (~31° S). Clim. Past 3 (1), 1–14. https://doi.org/10.5194/CP-3-1-2007.

Zech, R., May, J.H., Kull, C., Ilgner, J., Kubik, P.W., Veit, H., 2008. Timing of the late Quaternary glaciation in the Andes from ~ 15 to 40° S. J. Quat. Sci. 23 (6–7), 635–647. https://doi.org/10.1002/jqs.1200.